Microbuckling-field theory: a new model for material instabilities in cellular solids

Ryan C. McAvoy

Correspondence: rynomcavoy@berkeley.edu

Abstract: We introduce a general theory of the microbuckling field for modelling microbuckling and other material instabilities in cellular solids such as foams, lattices, and mechanical metamaterials. The model's main novelty lies in the assignment of a scalar-valued microbuckling field indicating the degree to which a material point is locally microbuckled. Two independent strain energies are prescribed: one for locally unbuckled and another for locally microbuckled material points. The former energy corresponds to linear elasticity of the underlying cells, while the latter to their microbuckling and eventual densification. These energies are constructed using standard Gibson-Ashby formulae for effective cellular solid constitutive parameters in terms the microstructural topology and composition. The microbuckling field unifies the pair of strain energies into a single overall energy *via* a first-order regularization of the microbuckling field, *i.e.*, including a penalty based on its normed gradient. Unlike existing continuum models for material instabilities, none of the strain energies need violate polyconvexity. In this manner, localized material behavior is described not by the absence of convexity but instead by the extended kinematic setting. The length scales conferred by the first-order regularization are precisely those relevant to the localized material behavior. We demonstrate that the model is amenable to both analytical and computational treatments and recovers phenomena distinctive of cellular solids such as localized compression bands and global softening mechanisms.

Keywords: Cellular solid, foam, lattice, microbuckling, material instability, modelling

Mathematics Subject Classification (2020): 74A35, 74A60, 74B20, 74S05

Contents

1 Introduction **2**

2 Stability and convexity **4**

3 Classical mechanics of cellular solids **6**
3.1 Relevant material properties 6
3.2 Architecture types 7
3.3 Linear elastic behavior 7
3.4 Nonlinear behavior 8
3.5 Buckingham pi theorem 9

4 Microbuckling-field theory **9**
4.1 Constitutive theory . . . 9
4.2 Variational theory . . . 12

5 Energy prescriptions **14**
5.1 Unbuckled energy density . . . 14
5.2 Microbuckled energy density . . . 14
5.2.1 Microbuckling criterion . . . 15
5.3 Tension-compression energy decomposition; total energy . . . 16

6 Legendre-Hadamard Inequality **17**

7 One-dimensional bar **20**

8 Simulations **22**
8.1 Uniaxial plane-strain compression . . . 23
8.2 Comparison with experimental data . . . 26
8.3 Indentation by a flat punch . . . 26

9 Future work **26**
9.1 Energy prescriptions . . . 26
9.2 Anisotropic microstructures . . . 28
9.3 Decoupled microbuckled and interface energies . . . 28
9.4 Dynamic effects . . . 29
9.5 Irreversibility . . . 29

10 Conclusions **29**

11 Declarations **30**

1 Introduction

Cellular solids – foams, lattices, and mechanical metamaterials – are ubiquitous in natural and artificial structures [1, 2]. In this paper, we define a cellular solid to be any material whose microstructure is characterized by an arrangement of small compartments separated by solid edges or faces [3]. The macroscale response of these solids is governed at the microscale by both the material comprising it – polymers, metals, ceramics, natural fibers, biominerals, *etc.* – as well as its cellular topology – periodic, aperiodic, open-celled, closed-celled, anisotropic, *etc.* Cellular solids often give rise to enhanced mechanical performance in the form of low weight combined with high stiffness and strength.

When cellular solids are placed under significant compressive loads, they exhibit peculiar mechanical behavior not seen in conventional 'dense' materials. At sufficient compression, the microstructural edges and faces undergo geometric buckling which leads to an immediate loss of local stiffness and a resulting plateau in the stress-strain response. This concept is referred to as elastic *microbuckling* by the structural engineering community [4]. Once a cellular solid is compressed far beyond the initial plateau in the stress-strain curve, it encounters the *densification* regime wherein the microstructural edges and struts come into contact and effectively reduce the amount of void space to zero. The material then exhibits a standard nonlinearly-elastic behavior with moduli belonging to the base material comprising the edges and faces [5]. While microbuckling can also

occur due to inelastic micromechanisms such as plastic yielding or fracture of the cellular topology, in this work we will be concerned primarily with elastic response.

There are several factors stimulating interest in the distinctive behavior of cellular solids. For example, it can be exploited in contemporary engineering applications such as wave dampeners [6,7], multistable materials [8], waveguides [9], energy absorption and energy dissipation [10–12], and energy trappers [13], among many others [14,15]. The general consensus is that the non-monotonic macroscopic stress-strain response resulting from microbuckling can be employed as a tool for design purposes in the spirit of the metamaterial paradigm [16]. Furthermore, microbuckling occurs naturally in many biological systems pertinent to the modern engineer, such as actin networks [17] and human tissue scaffolds [18]. The resulting compression bands are physical evidence of a material instability [4], the existence of which is prohibited by conventional strongly elliptic models for solid materials [19]. When dealing with material instabilities, the status quo of material modelling must be reconsidered [20, 21].

Most methods of capturing this peculiar behavior can be categorized according to discrete numerical modelling, homogenization, and non-monotonic continuum constitutive prescriptions. While discrete simulations of multiscale cellular solids offer the greatest fidelity, their implementation can be prohibitively expensive and may suffer from loss of convergence associated with standard nonlinear solvers incapable of negotiating global bifurcation, to say nothing of the formidable challenge of resolve multitudinous instances of microscale self-contact. Computational homogenization methods or other asymptotic micro-macro methods, which have received significant attention [22–32], aim to formulate a macroscopic energy that is equipped to handle such local microscale compression. However, they often also require appreciable computational resources due to the two-scale FE^2 nature of the simulations [33, 34], and multiscale approaches can still struggle with localization and transition regions [15]. Homogenization procedures are also inherently restricted to a select few user-chosen microstructures. Because cellular solids exhibit a myriad of distinct microstructures, this user-specific approach is unsuitable for analyzing arbitrary and general classes of these materials.

Given the shortcomings of the aforementioned approaches, non-monotonic continuum energy prescriptions have appeared as an attractive alternative for use in modelling cellular solids. The fundamental idea of this class of models rests on continuum strain energies which are by construction non-polyconvex, thereby permitting the existence of non-monotonic responses, energy wells, and bistable or metastable states. The concept was introduced in one dimensions by Ericksen [35] and has since been adapted to higher dimensional models, *e.g.*, [20, 21, 36–38]. Indeed, the use of these non-polyconvex models for modelling material instabilities in metamaterials is not new. Existing non-polyconvex models have been appended with gradient regularization in local volume change to produce well-defined compression bands [15], while non-monotonic continuum models have also been developed heuristically to describe instabilities as a solid-solid phase transformation [9,39,40]. However, such models are notably sparse in the literature in comparison to the wide variety of polyconvex models available. Furthermore, constitutive parameters appearing in such models are typically not amenable to direct physical interpretation. For example, many of these models are endowed with constitutive parameters tuning the non-convexity of the energy landscape, such as the location and size of energy wells. The question of how these parameters affect *quantifiable* observable response, *e.g.*, the stiffnesses of microbuckling material, or how they relate to known parameters of a cellular solid, *e.g.*, cell wall constitution and microscale length scales, remains unanswered in general.

The primary contribution of this paper is the introduction of a general and modular theory for microbuckling and other material instabilities in cellular solids that aims to fill the existing gap in the literature. The model draws inspiration from the multi-phase nature of the compressive

response. Rather than model microbuckling explicitly, we use a scalar phase field variable, called a *microbuckling field*, which represents the local level of microbuckling suffered by each material point. We assign this microbuckling field as an additional kinematic variable throughout the domain. Two standard constitutive models are prescribed: one for the initial elastic regime and a separate one for the combined microbuckled and densification regimes. Since these two regimes exhibit monotonic stress-strain curves independently, their constituent energies can satisfy any convexity or coercivity properties required by well-known existence theorems in nonlinear elasticity [19]. The microbuckling field is then used to combine the two strain energies together into a unified energy using appropriate convex functions and first-order regularization. This procedure renders the total strain energy non-convex in both unknown variables which leads to the nucleation and propagation of localized microbuckled bands. In summary, the salient goals of the proposed model are to:

1. recover the holistic compressive response for cellular solids;
2. remain constitutively faithful to the cellular microstructure;
3. remain analytically tractable;
4. facilitate straightforward computational implementation; and
5. permit the use of general strain energies.

On a historical note, the model is inspired by *tension-field theory* arising in the analysis of wrinkling in thin membranes under tension [41,42]. Both models concern genuine geometric instabilities – wrinkles in the case of tension-field theory and buckled cells in the case of microbuckling-field theory – manifesting due to the thin nature of the underlying microstructure and which, at the macroscale, would be otherwise prohibited by ellipticity requirements in standard continuum strain energies. Both models circumvent these ellipticity requirements by instead prescribing a modification, or relaxation, of the strain energy that furnishes the instabilities' macroscale effect without needing to explicitly model their geometry.

The paper is structured as follows. In Section 2, we discuss several notions of stability and convexity relevant to materials that exhibit microstructural instabilities and the elasticity models proposed to capture their behavior. In Section 3, we cursorily review established Gibson-Ashby constitutive laws pertinent to elastomeric cellular solids. In Section 4 we outline the microbuckling-field theory. Section 5 presents specific aspects of the associated constitutive theory, including details on its construction using the Gibson-Ashby parameters. Section 6 presents the novel Legendre-Hadamard ellipticity condition for the proposed system. In Section 7, we analytically investigate the behavior of a simple one-dimensional bar using the proposed theory. We implement the general theory in a finite-element setting in Section 8 and discuss the mechanics of a square specimen of a generic cellular solid under uniaxial unconfined plane-strain compression. The case of fixed supports, which induce localized microbuckling bands, and roller supports, which induce homogeneous microbuckling, are both considered. The influence of the primary constitutive parameters on the material response is quantified. Then, we test the performance of the model by comparing its predictions to experimental data on polyurethane open-cell foams. Finally, in Section 9 we discuss avenues for further refinement of the proposed theory and close in Section 10.

2 Stability and convexity

Microbuckling is commonly regarded as an example of a material instability and as such is precluded by the convexity conditions on the strain-energy function commonly assumed in conventional elas-

ticity. In the present section we recount some relevant notions of stability and convexity [19,43,44].

Consider a hyperelastic material with material points $\mathbf{X}$ occupying space in a fixed reference configuration κ. The material undergoes a deformation $\boldsymbol{\chi}$, which denotes the placement of points $\mathbf{x} = \boldsymbol{\chi}(\mathbf{X})$ in the deformed configuration κ_t. We suppress time in the following. We assume the material to be simple in the sense of Noll [45] and thus regard the local material response as depending only on the deformation gradient $\mathbf{F} = \nabla\boldsymbol{\chi}$, where $\nabla(\cdot)$ is the referential gradient operator. This local response is encoded in the strain energy density $\psi(\mathbf{F})$. The energy functional for this material is

$$E(\boldsymbol{\chi}) = \int_\kappa \psi(\mathbf{F}) dV - E_{ext}(\boldsymbol{\chi}), \tag{1}$$

where E_{ext} is the energy associated with conservative external actions. The energy criterion of elastic stability states that a deformation $\boldsymbol{\chi}$ is stable if and only if

$$E(\boldsymbol{\chi}) < E(\boldsymbol{\chi} + \boldsymbol{\delta\chi}), \tag{2}$$

where $\delta\boldsymbol{\chi}$ is a kinematically admissible deformation. It follows that $\boldsymbol{\chi}$ is an equilibrium deformation, *i.e.*, the first variation of (1) vanishes for any admissible $\delta\boldsymbol{\chi}$. A necessary condition for a state to be stable is that its second variation is positive, *i.e.*,

$$\delta^2 E = \int_\kappa \boldsymbol{\mathcal{M}}[\delta\mathbf{F}] \cdot \delta\mathbf{F} dV > 0, \tag{3}$$

where $\boldsymbol{\mathcal{M}} = \psi_{\mathbf{FF}}$ is the tensor of elastic moduli and $\delta\mathbf{F} = \nabla(\delta\boldsymbol{\chi})$. Material stability refers to whether (3) is locally satisfied with respect to rank-one perturbations in the deformation gradient:

$$\mathbf{a} \otimes \mathbf{n} \cdot \boldsymbol{\mathcal{M}}[\mathbf{a} \otimes \mathbf{n}] > 0, \tag{4}$$

where $\mathbf{a}, \mathbf{n}$ are arbitrary three-vectors. The condition (4) is called the strong ellipticity condition or the strict Legendre-Hadamard inequality and imposes a restriction on both the constitutive parameters and the underlying deformation. Physically, the condition ensures that small plane-wave perturbations of an underlying equilibrium deformation have real-valued wavespeeds and remain bounded in space and time, *i.e.*, that the equations of elastostatics are elliptic. It reflects the nature of the material itself and not the prescription of any initial or boundary data. Accordingly, when (4) is violated, we speak of a material instability. Such instabilities are qualitatively known to occur within the material itself and often exhibit a high degree of localization, *i.e.*, typically occurring within a small neighborhood of a material point, or when discontinuities in the deformation gradient are present.

Microbuckling can be regarded either as a geometric (*e.g.*, buckling) or material instability depending on the perspective adopted when observing the phenomenon. Of course, microbuckling is inherently related to genuine local buckling of the microstructure and therefore can be considered a geometric instability when the microstructure is discretely resolved. However, from the perspective of a macroscale continuum theory the geometric nature of the instability is lost in the upscaling process and in these cases the phenomenon is interpreted as a material instability, *i.e.*, it is encoded in the constitutive theory of the overall phenomenological continuum [22]. The present work proceeds from this latter perspective.

Existence theorems in nonlinear elasticity require the strain energy density to satisfy certain conditions of convexity. Ordinary convexity of ψ with respect to the deformation gradient $\mathbf{F}$, defined here as

$$\psi(\mathbf{F} + \nabla\boldsymbol{\zeta}) - \psi(\mathbf{F}) \geq \psi_{\mathbf{F}} \cdot \nabla\boldsymbol{\zeta}, \tag{5}$$

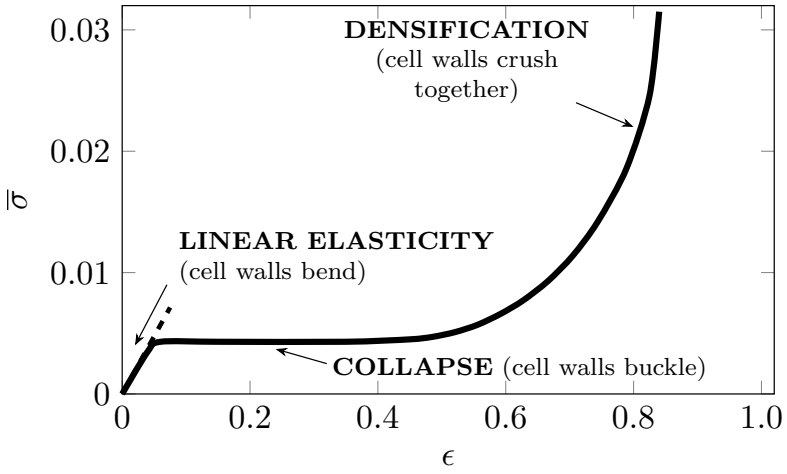

Figure 1: Compressive response of a typical elastic cellular solid.

where $\boldsymbol{\zeta}$ is any smooth vector field, can be ruled out on physical grounds. On the other hand, polyconvexity, in which the function $\psi(\mathbf{F})$ can be expressed as a function convex in the set $\{\mathbf{F}, \mathbf{F}^*, J\}$, where $\mathbf{F}^*$ is the cofactor and J is the determinant of $\mathbf{F}$, *i.e.*,

$$\psi(\mathbf{F}) = \Phi(\mathbf{F}, \mathbf{F}^*, J), \tag{6}$$

where Φ is convex in each argument, is a well established restriction on ψ and plays a major role in Ball's existence theory [46]. It is important to remark that (6) is a sufficient condition for (4) and therefore systems satisfying the former do not admit localized material behavior. Similarly, conventional models that admit such behavior necessarily violate (4) and (6). For this reason, conventional constitutive models for material instabilities have been proposed in the literature that violate polyconvexity conditions and stress-strain monotonicity, *e.g.*, [20, 21, 35–38], among others.

3 Classical mechanics of cellular solids

In this section, we summarize some aspects of the classical theory of cellular solids with emphasis on elastic open-celled bending-dominated architectures. The reader may consult the works of Gibson and Ashby for further information and details of the derivations mentioned here [1, 3, 5]. Aspects of more general architectures and inelastic effects will be pursued in upcoming reports.

3.1 Relevant material properties

It is natural to posit that the macroscale behavior of cellular solids depends on the microscale material parameters. For an isotropic open-celled architecture, the relevant parameters are the Young's modulus of the cell material E_s, the cell size l, and the cell edge thickness t. The ratio of the latter two parameters is proportional to the relative density of the solid ρ_{rel},

$$\rho_{rel} = \frac{\rho}{\rho_s} \propto \frac{t^2}{l^2} \in (0, 1), \tag{7}$$

where ρ is the density of the cellular solid and ρ_s is the density of the cell material. The saturation values $\rho_{rel} = 1$ and $\rho_{rel} = 0$ denote materials with no and only void space, respectively. As we will show below, a cellular solid's mechanical response is effectively characterized by E_s and ρ_{rel}.

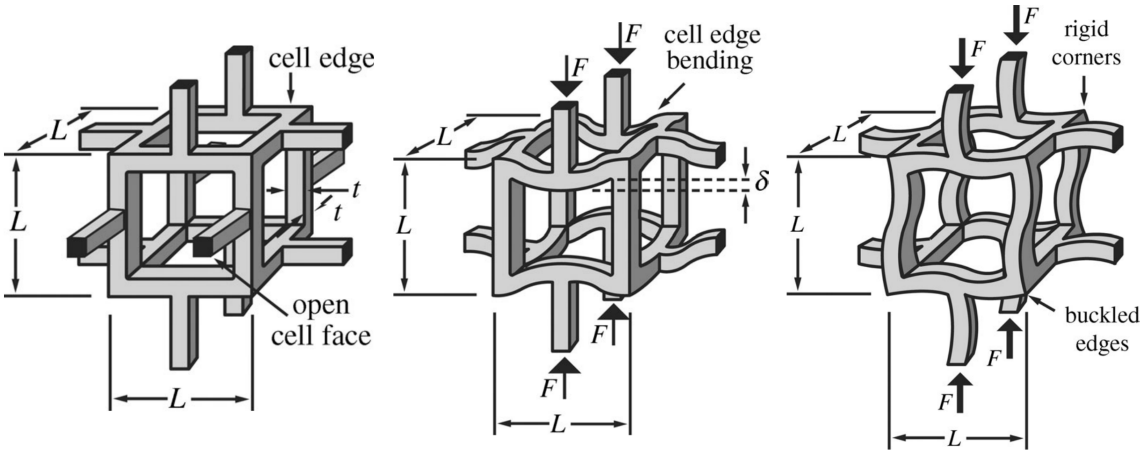

Figure 2: From left to right, an unloaded, loaded, and microbuckled idealized bending-dominated unit cell in an open-celled solid. The length scale L in the figure is called l in this report. Reproduced from [47] with permission.

3.2 Architecture types

Cellular solids can be either open-celled or closed-celled. In open-celled materials, the solid material is distributed in small struts which together comprise an arrangement of cells. In closed-cell solids, the solid material is distributed as small plates which together form cells that are closed off from one another. Within the class of open-celled solids it is also important to distinguish between bending-dominated and stretch-dominated architectures. In bending-dominated architectures, such as foams, cellular loads are primarily carried by bending of microscale struts as illustrated in Figure 2. In stretch-dominated architectures, such as lattices and architected metamaterials, cellular loads are primarily carried by axial compression of microscale struts. In this work, we will assume an open-celled bending-dominated cellular architecture to keep the content manageable. Extension to stretch-dominated and closed-cell architectures is straightforward in the given framework and will be investigated in an upcoming report; it entails replacing the following scaling laws by those relevant to the desired architecture; see, *e.g.*, [3, 47].

3.3 Linear elastic behavior

We begin by considering the nondimensionalized stress $\overline{\sigma}$ versus strain ϵ curve of a typical elastic cellular solid in Figure 1. For small compressive strain ϵ, the material behaves within a linear elastic regime in which the cells edges bend under loads applied around their midpoints as illustrated in Figure 2. This regime is governed by the macroscale Young's modulus E_U and shear modulus μ_U, where the subscripts $(\cdot)_U$ here and henceforth indicate 'unbuckled' for reasons that will soon be obvious. Using unit cell arguments, the effective macroscale Young's modulus E is calculated as

$$E_U = C_1 E_s \rho_{rel}^2, \tag{8}$$

where $C_1 \approx 1$ is a dimensionless fitting parameter [1]. Because shear deformation is also the macroscale realization of cell edge bending, the effective shear modulus μ_U scales like (8), *viz.*,

$$\mu_U = C_2 E_s \rho_{rel}^2, \tag{9}$$

where C_2 is another fitting constant.

C_1	C_2	C_3	C_4	C_5	C_6
1	3/8	0.05	1.4	0.4*	3/20*

Table 1: Broad estimates for the empirical fitting parameters in (8)-(13) when compared with experimental data for bending-dominated open-celled architectures. *No literature estimates exist for C_5 and C_6 as they have not been studied elsewhere to the author's knowledge, so the provided values are guesses *pro tempore*.

3.4 Nonlinear behavior

After the specimen reaches a sufficient compressive strain ϵ_M or stress σ_M, edges of the microscale cells geometrically buckle as depicted in Figure 2. This leads to an immediate loss of macroscale stiffness in which the curve becomes nearly flat for an extended range of strain as illustrated in Figure 1. This is called microbuckling or collapse. For this reason, ϵ_M and σ_M are called the microbuckling strain and stress, respectively, and appended subscripts $(\cdot)_M$ denote them as such. The scaling law for σ_M can be estimated by assuming that the individual struts comprising the cell undergo standard Euler buckling during the process, hence for another dimensionless fitting constant C_3,

$$\sigma_M = C_3 E_s \rho_{rel}^2. \tag{10}$$

After further compression, densification occurs. This is a purely geometric effect in which cell edges bend into one another, culminating in a 'dense' material with little or no void space. Any compression is transferred directly into the material comprising the cells, resulting in a dramatic increase in stiffness that diverges as the strain approaches a limiting value called the densification strain ϵ_D. Using geometric arguments, ϵ_D is calculated as

$$\epsilon_D = 1 - C_4 \rho_{rel}. \tag{11}$$

To the author's knowledge, no scaling laws exist for the effective Young's E_M and shear μ_M moduli relevant to this microbuckled and densification regime. However, we can adopt the reasonable assumption that they represent the stiffness associated with postbuckled deformation modes of the underlying microstructure. Since such modes primarily recruit bending deformation, we expect them to arise similar to those for E_U and μ_U, *i.e.*,

$$E_M = C_5 E_s \rho_{rel}^2, \tag{12}$$

and

$$\mu_M = C_6 E_s \rho_{rel}^2. \tag{13}$$

In summary, the mechanics of an elastic open-celled bending-dominated cellular solid can be quantified using the fundamental material parameters E_s and ρ_{rel} and empirical dimensionless fitting parameters $\{C_1, ..., C_6\}$ for the given solid, all of which are then used to prescribe the scaling laws (8)-(13). Broad experimental estimates for the empirical parameters C_i are listed in Table 1.

Remark: Many materials like wood, metal, ceramics, and certain plastics undergo plastic yielding or brittle fracture instead of elastic microbuckling at the onset of the collapse regime. Such effects could be imported in place of elastic microbuckling by replacing the microbuckling stress σ_M in (10) by the scaling law for plastic yield stress or brittle fracture stress. These latter laws depend differently on ρ_{rel} and recruit yield strength or fracture toughness of the cell wall material instead of E_s [47].

Remark: Much of the literature concerning finite deformation of cellular solids is restricted in the sense that the scaling laws (8)-(13) *by themselves* can be difficult to apply to arbitrary materials in general loading scenarios. In other words, a continuum energy functional recruiting the experimentally-tested estimates (8)-(13) and accounting for every regime of material response is absent. Such a model must delicately balance the opposing qualities of high micromechanical fidelity with simple implementation and analysis. This lacuna furnishes the impetus for the current work.

3.5 Buckingham pi theorem

A fundamental way to derive the scaling laws (8)-(13) without resorting to heuristic arguments is *via* the Buckingham pi theorem. For the bending-dominated open-celled architectures envisioned here, the flexure of cell edges drives effective moduli. If we idealize the edges as Euler-Bernoulli elastica, their flexure is codified in the flexural stiffness E_sI, where $I \propto t^4$ is the second moment of area. Thus (8)-(10), (12), and (13) must depend on E_st^4 and l, *e.g.*, $E_U = E_U(E_st^4, l)$. Simple application of the theorem furnishes,

$$E_U \propto \frac{E_st^4}{l^4} \propto E_s\rho_{rel}^2, \tag{14}$$

where the dimensionless constant C_1 can replace the latter proportionality with an equality. And so forth for the other parameters. In contrast, the densification strain ϵ_D, being a geometric quantity, is driven purely by the strut volume t^2l compared to the unit cell volume l^3, hence we must have $\epsilon_D = \epsilon_D(t^2l, l^3)$. The theorem yields the scaling law (11) after requiring $\lim_{\rho_{rel}\to 0} \epsilon_D = 1$.

4 Microbuckling-field theory

In this section, we introduce the concept of the microbuckling field and illustrate how it can be used to construct a model of microbuckling in cellular solids.

4.1 Constitutive theory

The primary difficulty with replicating the non-monotonic behavior illustrated in Figure 1 is that the vast majority of well-studied constitutive models, by virtue of their polyconvexity, are invariably materially stable and therefore cannot exhibit such a response. However, notice that the curve from Figure 1 can be cut into two sections: one corresponding to the linear elastic regime and one corresponding to the microbuckling and densification regime. Each of these sections are effectively monotonic in nature. An appropriate unification of these two regimes will recover the original non-monotonic response across the entire range of strain. To accommodate this behavior, we propose two strain-energy densities: the unbuckled strain energy ψ_U corresponding to the linear elastic regime and the microbuckled strain energy ψ_M corresponding to the microbuckled and densification regime.

A smooth scalar field $\varphi \in [0, 1]$, called the *microbuckling field*, is introduced throughout the domain as an additional unknown quantity to be solved together with the deformation map $\boldsymbol{\chi}$. The microbuckling field is restricted to have values between zero and one, with a value of zero corresponding to a material point being locally unbuckled and a value of one to a material point being completely microbuckled. Figure 3 illustrates this concept. We propose a unified strain energy density with respect to the reference configuration,

$$\psi(\mathbf{F}, \varphi) = f_U(\varphi)\psi_U(\mathbf{F}) + f_M(\varphi)\psi_M(\mathbf{F}), \tag{15}$$

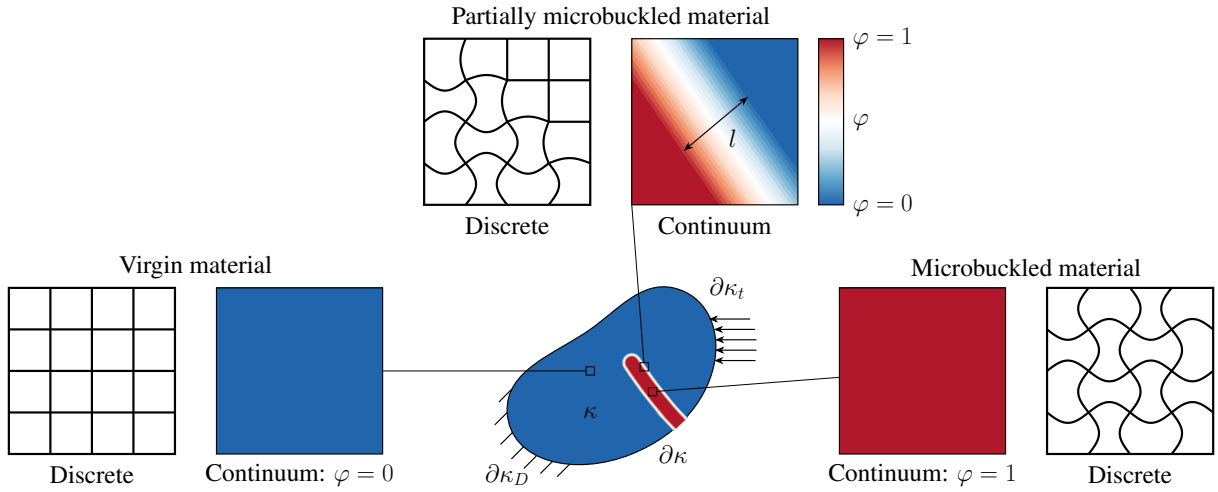

Figure 3: A partially microbuckled cellular solid with depictions of localized discrete microbuckling and its continuum interpretation *via* the microbuckling field $\varphi \in [0, 1]$.

which notably admits as functional arguments both the deformation map and the microbuckling field. The dimensionless functions f_U and f_M effectively quantify the spatial distribution for the unbuckled and microbuckled regimes, respectively, and thus their interplay determines the degree to which a material point responds according to the unbuckled energy ψ_U or the microbuckled energy ψ_M. When the microbuckling field is locally zero, the total strain energy density collapses onto the unbuckled strain energy density, *i.e.*,

$$\psi(\mathbf{F}, 0) = \psi_U(\mathbf{F}), \tag{16}$$

and, similarly, when the microbuckling field is locally unity, the total strain energy density collapses onto the microbuckled energy density:

$$\psi(\mathbf{F}, 1) = \psi_M(\mathbf{F}). \tag{17}$$

The equations (16) and (17) imply that

$$f_U(0) = 1, \quad f_U(1) = 0, \quad f_U'(1) = 0, \quad f_M(1) = 1, \quad f_M(0) = 0, \quad f_M'(0) = 0, \tag{18}$$

where the third and sixth equations ensure that f_U (resp. f_M) is saturated when the microbuckling (resp. unbuckled) regime is attained. We also require that f_U be monotonically decreasing, *i.e.*, $f_U' \leq 0$, so that ψ_U decreases as a material point becomes more microbuckled. A suitable candidate for f_U is the simple convex function

$$f_U = (1 - \varphi)^2, \tag{19}$$

and we adopt the following form for f_M,

$$f_M = \varphi^2 + \frac{l^2}{4}|\nabla\varphi|^2, \tag{20}$$

where l is a length scale parameter characterizing the size of the underlying microstructure, *e.g.*, the cell size. To motivate the choices (19) and (20) geometrically, consider a canonical microbuckling

band generated in a crushed honeycomb specimen in Figure 4, in which we plot below each specimen's deformed shape a one-dimensional line plot made from a horizontal cut along the direction of compression. Initially, when the sample is undeformed, the material is unbuckled and φ vanishes across the cut. Eventually, a local band of cells collapses at $x = 0$, with $\varphi(0) = 1$ and a sufficiently smooth decay down to $\varphi = 0$ over a length scale l characterizing the microstructure. As further compression occurs, the microbuckled region expands while the transition region retains the same decay distance l. If we denote the unbuckled and microbuckled regions as κ_U and κ_M, respectively, then the total energy is written as

$$E = \int_{\kappa_U} \psi_U dx + \int_{\kappa_M} \psi_M dx + E_T, \tag{21}$$

where E_T accounts for energy of the transition region wherein $d\varphi/dx \neq 0$. Since κ_U is only where $\varphi = 0$, we can utilize the compact support function $f_U = (1-\varphi)^2$ to recast the domain of integration of the former integral over the entire material body κ; similarly, we can use the compact support function φ^2 to recast integration over κ_M instead over κ, *viz.*:

$$E = \int_{\kappa} \left(f_U \psi_U + \varphi^2 \psi_M \right) dx + E_T. \tag{22}$$

Now, if we regard the transition region as a diffuse extension of κ_M, then we can account for its energetic contributions by appending φ^2 in (21) with a term nonzero over the former. This would be precisely $d\varphi/dx$, but we additionally square it in order to penalize only its magnitude, scale it by the concomitant length scale l to make it dimensionally consistent, and scale it by $\Delta < 1$ to expedite its small contributions compared to φ^2. Thus, $E_T = \int_\kappa \Delta l^2 (d\varphi/dx)^2 \psi_M dx$, and therefore the total energy (22) can be rewritten as

$$E = \int_{\kappa} \left(f_U \psi_U + f_M \psi_M \right) dx, \tag{23}$$

where $f_M = \varphi^2 + l^2(d\varphi/dx)^2/4$ with $\Delta = 1/4$. Generalizing to three dimensions induces the strain energy density (15) with compact support, or spatial distribution, functions (19) and (20), as desired. The reasons for the import of the first-order regularization $l^2|\nabla\varphi|^2/4$ into the system are twofold: first, to account for the energy of the transition region, and second, to generate a smooth spatial transition between unbuckled and microbuckled states. Alternative formulations of ψ are discussed in Section 9. Note that the functional form for f_M has geometric origins, while that for f_U is more empirical in nature. Indeed, (19) is a simple modelling choice; any f_U is technically suitable as long as it satisfies (18) and other empirical forms are investigated in the adjacent phase-field fracture literature where they are denoted g and called degradation functions [48]. Furthermore, the choice of $\Delta = 1/4$ is a largely arbitrary model decision that could be worthy of additional study down the road.

Remark: The functions f_U and f_M in (19) and (20), respectively, do not satisfy the partition of unity with respect to φ. In other words, for spatially homogeneous φ, we have

$$f_U + f_M = \varphi^2 + (1-\varphi)^2 \neq 1. \tag{24}$$

Partitions of unity are characteristic of mixture theories in which the microbuckling field would represent volume fractions and f_U would be of the form

$$f_U = 1 - \varphi^2. \tag{25}$$

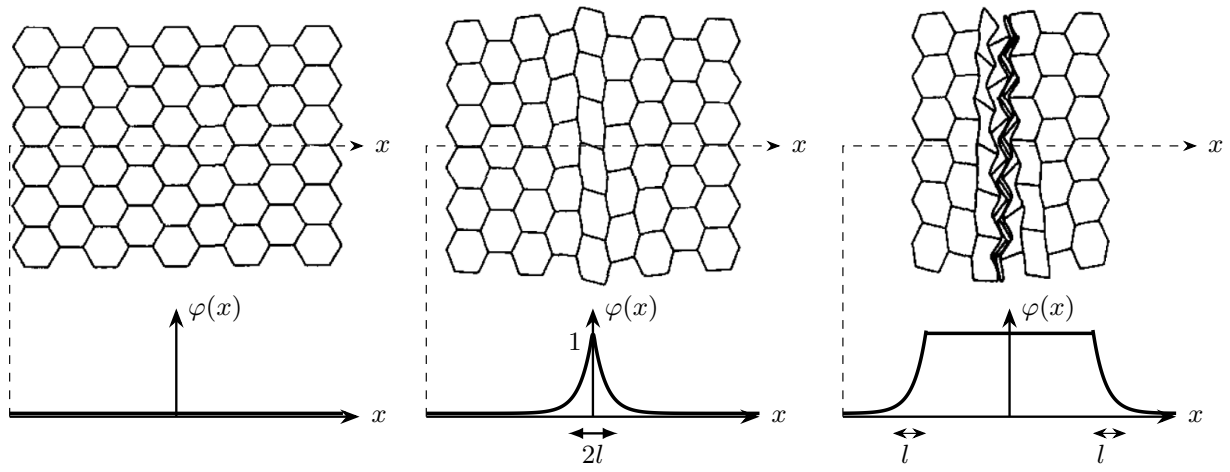

Figure 4: Microbuckling field evolution during in-plane crushing of honeycomb. Specimen images taken from [49].

However, this fails to satisfy the saturation condition $f_U'(1) = 0$. Further, we found in simulations using the form (25) that the microbuckling field failed to move off of the trivial solution $\varphi = 0$. This is possibly associated with the observation that (25) satisfies $f_U'(0) = 0$, which can hinder the nucleation of nontrivial values of φ, while (19) satisfies $f_U'(0) = -2$ and therefore promotes the nucleation of nontrivial values of φ. We adopt henceforth the version (19) primarily due to its geometric underpinnings; an alternative theory to that presented here can be proposed using support functions satisfying partition of unity, *e.g.*, (25), though effort must be spent in rectifying the poor performance mentioned above.

Remark: The present model can be considered a variant of the general theory of *pseudo-elasticity* developed for the analysis of materials whose strain energy function changes during deformation [50].

4.2 Variational theory

The total energy of the system can be written using (1) with (15),

$$E(\boldsymbol{\chi}, \varphi) = \int_\kappa \left[g(\varphi)\psi_U(\mathbf{F}) + f_M(\varphi)\psi_M(\mathbf{F}) \right] dV - E_{ext}(\boldsymbol{\chi}), \tag{26}$$

and henceforth we suppress the arguments for convenience. We assume equilibria are those states that render the functional (26) stationary with respect to admissible variations. The spaces of admissible deformations and microbuckling fields are defined respectively as

$$\mathcal{V} = \left\{ \boldsymbol{\chi} \in \left[H^1(\kappa) \right]^d \mid \boldsymbol{\chi} = \overline{\boldsymbol{\chi}} \text{ on } \partial\kappa_D \right\}, \tag{27}$$

and

$$\mathcal{P} = \left\{ \varphi \in H^1(\kappa) \mid \varphi = \overline{\varphi} \text{ on } \partial\kappa_P \right\}, \tag{28}$$

where $H^1(\kappa)$ is the Sobolev space of scalar-valued square-integrable functions with square-integrable first-order derivatives and d denotes the dimension of the physical space. Here, $\overline{\boldsymbol{\chi}}$ is the Dirichlet boundary condition prescribed for the deformation on a subsection of the boundary $\partial\kappa_D \subset \partial\kappa$; similarly for the microbuckling field. The test spaces of admissible variations, in which the relevant

functions vanish on the Dirichlet portion of the boundary, are denoted by $\mathcal{V}_0$ and $\mathcal{P}_0$. Consider a one-parameter family of admissible fields $\{\boldsymbol{\chi}(\epsilon), \varphi(\epsilon)\} \in \mathcal{V} \times \mathcal{P}$ and let $\delta(\cdot) = \frac{d}{d\epsilon}(\cdot)|_{\epsilon=0}$ denote a variational derivative. Since equilibria render (26) stationary, we must have that $\forall\{\delta\boldsymbol{\chi}, \delta\varphi\} \in \mathcal{V}_0 \times \mathcal{P}_0$,

$$\delta E = 0, \tag{29}$$

where

$$\delta E = \int_\kappa \left[\delta f_U \psi_U + f_U \delta\psi_U + \delta f_M \psi_M + f_M \delta\psi_M\right] dV - \delta E_{ext}. \tag{30}$$

For a conservative external loading consisting of body forces $\mathbf{b}$ and applied surface tractions $\mathbf{p}$, the external virtual work is expressible in the form

$$\delta E_{ext} = \int_\kappa \mathbf{b} \cdot \delta\boldsymbol{\chi} dV + \int_{\partial\kappa_p} \mathbf{p} \cdot \delta\boldsymbol{\chi} dA, \tag{31}$$

where $\partial\kappa_p$ is the section of the reference boundary where tractions are specified. Using (19) and (20) yields the total weak form in terms of the pairwise unknown field, $\{\boldsymbol{\chi}, \varphi\}$

$$\delta E = \int_\kappa \left[\mathbf{P} \cdot \nabla(\delta\boldsymbol{\chi}) + \left(f_U' \psi_U + \varphi\psi_M\right)\delta\varphi + l^2 \nabla\varphi \cdot \nabla(\delta\varphi)\psi_M\right] dV - \delta E_{ext}, \tag{32}$$

where we have defined $\mathbf{P} = \psi_{\mathbf{F}} = f_U \mathbf{P}_U + f_M \mathbf{P}_M$ with $\mathbf{P}_U = (\psi_U)_{\mathbf{F}}$ and $\mathbf{P}_M = (\psi_M)_{\mathbf{F}}$. After integrating by parts the expression for δE reduces to

$$\begin{aligned} \delta E = &\int_\kappa \left\{\mathrm{Div}\mathbf{P} \cdot \delta\boldsymbol{\chi} + \left[f_U' \psi_U + \varphi\psi_M - l^2 \mathrm{Div}(\nabla\varphi\psi_M)\right]\delta\varphi\right\} dV \\ &+ \int_{\partial\kappa} \left[\mathbf{P}\mathbf{N} \cdot \delta\boldsymbol{\chi} + \psi_M \frac{\partial\varphi}{\partial N}\delta\varphi\right] dA - \delta E_{ext}, \end{aligned} \tag{33}$$

where $\mathrm{Div}(\cdot)$ is the referential divergence operator, $\mathbf{N}$ is the exterior unit normal to the boundary, and $\partial(\cdot)/\partial N$ is the normal derivative. Since the variations $\delta\boldsymbol{\chi}$ and $\delta\varphi$ are independent, we can split (33) into two equations. Thus, we seek $\boldsymbol{\chi} \in \mathcal{V}$ and $\varphi \in \mathcal{P}$ such that for every $\delta\boldsymbol{\chi} \in \mathcal{V}_0$ and $\delta\varphi \in \mathcal{P}_0$,

$$\begin{aligned} \int_\kappa (\mathrm{Div}\mathbf{P} + \mathbf{b}) \cdot \delta\boldsymbol{\chi} dV &= \int_{\partial\kappa_p} (\mathbf{P}\mathbf{N} - \mathbf{p}) \cdot \delta\boldsymbol{\chi} dA, \\ \int_\kappa \left(f_U' \psi_U + \varphi\psi_M - l^2 \mathrm{Div}(\nabla\varphi\psi_M)\right)\delta\varphi dV &= \int_{\partial\kappa} \psi_M \frac{\partial\varphi}{\partial N}\delta\varphi dA. \end{aligned} \tag{34}$$

The fundamental lemma of the calculus of variations then furnishes the Euler-Lagrange equations holding in κ,

$$\mathrm{Div}\mathbf{P} + \mathbf{b} = \mathbf{0} \quad \text{and} \quad f_U' \psi_U + \varphi\psi_M - l^2 \mathrm{Div}(\nabla\varphi\psi_M) = 0, \tag{35}$$

and the associated natural boundary conditions,

$$\mathbf{P}\mathbf{N} = \mathbf{p} \ \text{ on } \ \partial\kappa_p \quad \text{and} \quad \partial\varphi/\partial N = 0 \ \text{ on } \ \partial\kappa \setminus \partial\kappa_P. \tag{36}$$

The first equation in (35) is standard elastostatics while the second corresponds to the diffusive spatial evolution of the microbuckling field. It is also important to note that the system is fully coupled in the sense that both $\boldsymbol{\chi}$ and φ appear in each equation of (35).

Remark: The split weak form follows from integrating by parts the equations in (34) to reduce the differentiability required of the trial function spaces. This yields the two independent residual equations

$$\begin{aligned} &\int_\kappa \mathbf{P}\cdot\nabla\delta\boldsymbol{\chi}dV - \int_\kappa \mathbf{b}\cdot\delta\boldsymbol{\chi}dV - \int_{\partial\kappa_p}\mathbf{p}\cdot\delta\boldsymbol{\chi}dA = 0 \\ &\int_\kappa \left[\left(f_U'\psi_U + \varphi\psi_M\right)\delta\varphi + l^2\nabla\varphi\cdot\nabla(\delta\varphi)\psi_M\right]dV = 0, \end{aligned} \tag{37}$$

which are later implemented in the staggered finite element scheme in Section 8.

5 Energy prescriptions

The prescription of constitutive models should be done in a manner faithful to the microstructure at hand. In this section, we describe the means by which microbuckling-field theory can recruit the customary Gibson-Ashby scaling laws (8)-(13) to fully prescribe ψ_U and ψ_M.

5.1 Unbuckled energy density

We begin with the unbuckled strain energy ψ_U. Since this regime only exhibits standard linearly-elastic responses, we can simply prescribe any elastic constitutive law. In the case of isotropy, a compressible neo-Hookean model suffices for our purposes [51]:

$$\psi_U = \frac{\mu_U}{2}\sum_{i=1}^{d} U_{NH}(\Lambda_i) + \frac{\lambda_U}{4}U_{NH}(J), \tag{38}$$

where $\Lambda_i = \sqrt{\det\mathbf{F}^\mathbf{T}\mathbf{F}}$ are the principal strains, $J = \det\mathbf{F}$, the scalar function U_{NH} is defined as

$$U_{NH}(s) = s^2 - 1 - 2\,\ln s, \tag{39}$$

and λ_U is the first Lamé parameter given by

$$\lambda_U = \frac{\mu_U(E_U - 2\mu_U)}{3\mu_U - E_U}. \tag{40}$$

We have already established scaling laws for the effective moduli in this regime, E_U in (8) and μ_U in (9), so these formulae can simply be inserted into (38).

5.2 Microbuckled energy density

Construction of ψ_M is more subtle. Notice that the collapse regime remains around a target stress value in Figure 1. We idealize this as the microbuckling stress σ_M previously derived in (10). We postulate that the microbuckling stress σ_M, being envisioned as the stress required to microbuckle a material point within a uniaxial setting [3], can be generalized to three dimensions using a constant strain energy density $\mathcal{G}_M$ that, alternatively, represents the local strain energy density required to microbuckle a unit volume of material; mathematically, $\mathcal{G}_M$ entails an energy barrier that must be locally overcome in order for microbuckling to occur. Therefore, the microbuckled strain energy ψ_M must be, at minimum, this energy density value $\mathcal{G}_M$. Conveniently, $\mathcal{G}_M$ has the same units as E_s, so by using the Buckingham pi theorem discussed in Section 3, it can be determined from the scaling law

$$.\mathcal{G}_M = C_7 E_s \rho_{rel}^2, \tag{41}$$

for some constant C_7. The densification regime, following collapse in Figure 1, exhibits a very slow onset of stiffness that diverges as the densification strain ϵ_D is approached. Using (11), we propose that this is effectively equivalent to locally attaining the densification stretch

$$\Lambda_D = 1 - \epsilon_D = C_4 \rho_{rel}. \tag{42}$$

Therefore, it is appropriate to append the base microbuckling energy density $\mathcal{G}_M$ with a strain energy density function that vanishes at unity but diverges in the vicinity of Λ_D. We will utilize an logarithmic densification function to this end,

$$U_{dens}(s;\tau) = -2(1-\tau)^2 \ln\left(1 - \left[\frac{1-s}{1-\tau}\right]^2\right), \tag{43}$$

which satisfies $U_{dens}(1;\tau) = 0$ and $\lim_{s\to\tau} U_{dens} = \infty$. The selection (43) is not authoritative but rather a simple model choice; the effect of using alternative densification functions instead of (43) is studied in the supplementary material. We construct an energy density using the densification function (43) which diverges (a material point densifies) if any principal stretch Λ_i approaches its crushing limit Λ_D or the volumetric compression J approaches geometric densification Λ_D^d:

$$\psi_M^{dens} = \frac{\mu_M}{2} \sum_{i=1}^{d} U_{dens}(\Lambda_i;\Lambda_D) + \frac{\lambda_M}{4} U_{dens}(J;\Lambda_D^d). \tag{44}$$

Thus, densification occurs on both the deviatoric and volumetric energy contributions. The moduli in (44) refer to μ_M, whose scaling law is given by (13), and the first Lamé parameter λ_M

$$\lambda_M = \frac{\mu_M(E_M - 2\mu_M)}{3\mu_M - E_M}, \tag{45}$$

where E_M is obtained from the scaling law (12). The resulting microbuckled energy density is simply the additive combination of $\mathcal{G}_M$ and (44):

$$\psi_M = \mathcal{G}_M + \frac{\mu_M}{2} \sum_{i=1}^{d} U_{dens}(\Lambda_i;\Lambda_D) + \frac{\lambda_M}{4} U_{dens}(J;\Lambda_D), \tag{46}$$

which can be fully prescribed after inserting (11), (41), (42), and (45).

Remark: The prescription (44) is rather speculative and relies primarily on physical intuition. Little exists in the literature in the way of offering empirical or heuristic estimates for this energetic contribution.

5.2.1 Microbuckling criterion

Since $\mathcal{G}_M$ is the energy density required to microbuckle a material point, we can therefore regard microbuckling as occurring when the energy state prior to microbuckling, ψ_U, attains this value:

$$\psi_U|_{\mathbf{F}_M} = \mathcal{G}_M. \tag{47}$$

This is the *microbuckling criterion* indicating when it is energetically preferable for a material point to transition into the microbuckled state. In writing (48) we have evaluated both energies at the underlying local deformation state at the onset of microbuckling, $\mathbf{F}_M$. If we suppose the energy is continuous across microbuckling, *i.e.*,

$$\psi_U|_{\mathbf{F}_M} = \psi_M|_{\mathbf{F}_M}, \tag{48}$$

which is reasonable within the present hyperelastic setting, and insert this into (47), we obtain

$$\psi_M^{dens}|_{\mathbf{F}_M} = 0, \tag{49}$$

which is a *restriction* on the microbuckled densification energy, signifying that all local energy when critically microbuckled is due to Euler buckling of the struts. We envision two possible ways to enforce (49). The first is to pose $\mathbf{F}_M$ as a zero-energy symmetry transformation:

$$\psi_M^{dens}(\mathbf{F}) = \psi_M^{dens}(\mathbf{F}\mathbf{F}_M^{-1}), \tag{50}$$

and since $\mathcal{G}_M$ is constant, the microbuckled strain energy (46) is replaced by

$$\psi_M(\mathbf{F}) = \psi_M(\mathbf{F}\mathbf{F}_M^{-1}). \tag{51}$$

A consequence of (50) is that the state $\mathbf{F}_M$ is locally stress free. A second way is to simply offset the energy by $\psi_M|_{\mathbf{F}_M}$, *i.e.*, $\psi_M \mapsto \psi_M - \psi_M|_{\mathbf{F}_M}$. We proceed with (51) in this report but anticipate this could be be worthy of further study in due course.

One way to determine the critical microbuckled deformation state $\mathbf{F}_M$ for use in (51) is to utilize the criterion (47). However, this is one scalar equation whose solution $\mathbf{F}_M$ lives in the manifold Lin^+ of dimension d^2; the problem as stated is not well-posed for $d > 1$. A simpler alternative is to assume that $\mathbf{F}_M$ is isotropic with a critical microbuckling compressive stretch Λ_M:

$$\mathbf{F}_M = \Lambda_M \mathbf{I}. \tag{52}$$

Since (52) is fully prescribed by a single scalar Λ_M, the problem of determining $\mathbf{F}_M$ with (47) becomes well-posed. We proceed under the modelling assumption (52) for the reasons that it allows us to explicitly solve for $\mathbf{F}_M$ and because there are no indications of directionality within the energies to begin with. However, it is an exception, not a norm, and a more mechanistically-motivated choice is a natural path for future work. In the case of (52), we can determine Λ_M uniquely using (47). Indeed, let $\psi_U(\Lambda) = \psi_U|_{\mathbf{F}=\Lambda\mathbf{I}}$. Since $0 = \psi_U(1) < \mathcal{G}_M$, $\lim_{\Lambda\to 0}\psi_U = \infty$, and ψ_U is monotonically increasing as Λ decreases from unity, the intermediate value theorem guarantees that (47) admits a unique solution $\Lambda_M \in (0,1)$. In this case, (51) is replaced by

$$\psi_M = \mathcal{G}_M + \frac{\mu_M}{2}\sum_{i=1}^{d} U_{dens}(\tilde{\Lambda}_i;\tilde{\Lambda}_D) + \frac{\lambda_M}{4}U_{dens}(\tilde{J};\tilde{J}_M), \tag{53}$$

where $\tilde{\Lambda} = \Lambda/\Lambda_M$, $\tilde{J} = J/\Lambda_M^d$, *etc.*, and $J_M = \det\mathbf{F}_M = \Lambda_M^d$.

Remark: Microbuckling occurs at small strains. Since ψ_M^{dens} is intended to only capture response near ϵ_D, energetic contributions of $\psi_M^{dens}|_{\mathbf{F}_M}$ may be negligible in which case (49) can be disregarded.

5.3 Tension-compression energy decomposition; total energy

Microbuckling primarily occurs in compression. To prevent the emergence of microbuckling bands as a result of tensile loads, we utilize a tensile-compressive split of the energy. This principle and its prescription have been well-studied in the context of phase-field fracture [52–55] and we will follow the approach outlined in [52] to this end. Compressive $\Lambda_i^- < 1$ and tensile $\Lambda_i^+ > 1$ parts of a principal stretch Λ_i are defined as

$$\Lambda_i^{\pm} = \frac{\Lambda_i + 1 \pm |\Lambda_i - 1|}{2} = \begin{cases} \Lambda_i & \Lambda_i \gtrless 1 \\ 1 & \text{else} \end{cases} \tag{54}$$

The compressive J^- and tensile J^+ volume changes are defined in a similar manner. Since only the compressive strains contribute to microbuckling, we only account for the energies resulting from them in ψ_M and require that the energy resulting from tensile strains is insensitive to the microbuckling field and behaves as a standard energy. If we use the notation

$$\psi^{\pm} = \psi(\Lambda^{\pm}, J^{\pm}), \tag{55}$$

then the consequent total energy decomposition is

$$\psi = f_U \psi_U^- + f_M \psi_M^- + \psi_U^+. \tag{56}$$

The equation (56) is the complete energy characterizing the cellular solid and can be fully prescribed using (38) and (53) with constitutive parameters incorporating the established scaling laws (8)-(13) and (41). Also note that the energy (56) can be nondimensionalized by E_s because all parameters with dimensions of stress are linearly dependent on E_s.

Remark: An advantage of the current model is that *any* constitutive models can be used to describe the unbuckled and microbuckled regimes; this contrasts with alternative formulations which must necessarily be non-polyconvex. Indeed, the class of constitutive models proposed for each regime is not restricted to be of a first-gradient or simple type [45]. Generalized continuum theories have the ability to exhibit nonstandard mechanical behavior distinctive of microstructured materials. For example, higher gradient models, such as second gradient and strain gradient models [16, 56–59], as well higher order models, such as the Cosserat and micromorphic models [60–68], are equally valid to use in the energy functional (26).

6 Legendre-Hadamard Inequality

In this section, we discuss the Legendre-Hadamard condition. This pointwise condition places a restriction on both the field variables $\{\boldsymbol{\chi}, \varphi\}$ and the constitutive model and must be satisfied by minimizing equilibria everywhere in the domain. If any set of fields for a given model fail to satisfy this condition at any given material point, then such an equilibrium state does not minimize the energy and is therefore unstable according to the energy criterion (2). In the following derivation we make extended use of techniques presented in [44, 69]. Recall the total energy functional (26),

$$E = \int_\kappa \left[f_U \psi_U + f_M \psi_M \right] dV - E_{ext}(\boldsymbol{\chi}). \tag{57}$$

Without loss of generality, the integrand in (57) can be modified in a manner consistent with (56). Consider a one-parameter family $\{\boldsymbol{\chi}(\epsilon), \varphi(\epsilon)\}$ of kinematically admissible states and suppose $\{\boldsymbol{\chi}(0), \varphi(0)\}$ are energy minimizers. The first variation is given by (30) which we rewrite here using (20) and (19) as

$$\delta E = \int_\kappa \left[2\left\{ (\varphi - 1)\psi_U + \varphi \psi_M \right\} \delta\varphi + (l^2/2)\psi_M \nabla\varphi \cdot \nabla(\delta\varphi) + \mathbf{P} \cdot \delta\mathbf{F} \right] dV - \delta E_{ext} = 0, \tag{58}$$

where the second equality follows as the underlying configuration is assumed to be an equilibrium state. We take another variation on (58), which, after some rearrangement, yields

$$\begin{aligned} \delta^2 E = &\int_\kappa \left[2\left\{ (\varphi - 1)\psi_U + \varphi \psi_M \right\} \delta^2\varphi + (l^2/2)\psi_M \nabla\varphi \cdot \nabla(\delta^2\varphi) + \mathbf{P} \cdot \delta^2\mathbf{F} \right] dV - \delta E_{ext} \\ &+ \int_\kappa \left[2(\psi_U + \psi_M)(\delta\varphi)^2 + (l^2/2)\psi_M \nabla(\delta\varphi) \cdot \nabla(\delta\varphi) + \delta\mathbf{F} \cdot \boldsymbol{\mathcal{M}} \left[\delta\mathbf{F}\right] \right] dV \\ &+ \int_\kappa \left[4\left\{ (\varphi - 1)\mathbf{P}_U + \varphi \mathbf{P}_M \right\} \cdot \delta\mathbf{F}\delta\varphi + l^2 \left\{ \nabla\varphi \cdot \nabla(\delta\varphi) \right\} \mathbf{P}_M \cdot \delta\mathbf{F} \right] dV \geq 0, \end{aligned} \tag{59}$$

where the inequality necessarily follows from the premise of energy minimization, cf. (3), and

$$\boldsymbol{\mathcal{M}} = \psi_{\mathbf{FF}} = g(\psi_U)_{\mathbf{FF}} + f_M(\psi_M)_{\mathbf{FF}}. \tag{60}$$

Since the underlying state is equilibrated, the first line in (59) vanishes, and thus (59) reduces to

$$\begin{aligned}\delta^2 E = &\int_\kappa \left[2(\psi_U + \psi_M)(\delta\varphi)^2 + (l^2/2)\psi_M \nabla(\delta\varphi)\cdot\nabla(\delta\varphi) + \delta\mathbf{F}\cdot\boldsymbol{\mathcal{M}}\left[\delta\mathbf{F}\right]\right] dV \\ &+ \int_\kappa \left[4\left\{(\varphi-1)\mathbf{P}_U + \varphi\mathbf{P}_M\right\}\cdot\delta\mathbf{F}\delta\varphi + l^2\left\{\nabla\varphi\cdot\nabla(\delta\varphi)\right\}\mathbf{P}_M\cdot\delta\mathbf{F}\right] dV \geq 0.\end{aligned} \tag{61}$$

Consider the class of variations

$$\delta\boldsymbol{\chi} = \varepsilon\boldsymbol{\xi}(\mathbf{Z}), \quad \delta\varphi = \varepsilon\eta(\mathbf{Z}), \quad \mathbf{Z} = (\mathbf{X} - \mathbf{X}_0)/\varepsilon, \tag{62}$$

where $\mathbf{X}_0 \in \kappa$ is a fixed interior reference point, $\varepsilon > 0$ is a small positive constant, and $\boldsymbol{\xi}(\mathbf{Z})$ and $\eta(\mathbf{Z})$ are compactly supported in the image $\mathcal{D}$ of a strictly interior region $\kappa' \subset \kappa$ under the mapping $\mathbf{Z}(\cdot)$. Consequently the variations $\delta\boldsymbol{\chi}$ and $\delta\varphi$ vanish on the boundary $\partial\kappa$ and are therefore admissible. The variations (62) allows us to restrict attention to a small domain surrounding a given material point and consequently only consider the terms which appear at leading order. To this end, combining (62) with (61) and exchanging the region of integration yields

$$\begin{aligned}&\varepsilon^3\int_{\mathcal{D}}\left[2(\psi_U+\psi_M)\varepsilon^2\eta^2 + (l^2/2)\psi_M\nabla_Z\eta\cdot\nabla_Z\eta + \nabla_Z\boldsymbol{\xi}\cdot\boldsymbol{\mathcal{M}}\left[\nabla_Z\boldsymbol{\xi}\right]\right] dV_Z \\ &+\varepsilon^3\int_{\mathcal{D}}\left[4\varepsilon\left\{(\varphi-1)\mathbf{P}_U+\varphi\mathbf{P}_M\right\}\cdot\eta\nabla_Z\boldsymbol{\xi} + l^2(\nabla\varphi\cdot\nabla_Z\eta)\mathbf{P}_M\cdot\nabla_X\boldsymbol{\xi}\right] dV_Z \geq 0,\end{aligned} \tag{63}$$

where $\nabla_Z(\cdot) = \partial(\cdot)/\partial\mathbf{Z} = \varepsilon^{-1}\nabla(\cdot)$ and we have used $dV = \varepsilon^3 dV_Z$. It is understood in (63) that all functions of $\mathbf{X}$ are evaluated on $\mathbf{X}(\mathbf{Z}) = \varepsilon\mathbf{Z} + \mathbf{X}_0$. Dividing (63) by ε^3 and passing to the limit $\varepsilon \to 0$ furnishes

$$\int_{\mathcal{D}}\left[(l^2/2)|\nabla_Z\eta|^2\psi_M + \nabla_Z\boldsymbol{\xi}\cdot\boldsymbol{\mathcal{M}}[\nabla_Z\boldsymbol{\xi}] + l^2(\nabla\varphi\cdot\nabla_Z\eta)\mathbf{P}_M\cdot\nabla_X\boldsymbol{\xi}\right] dV_Z \geq 0, \tag{64}$$

where $\boldsymbol{\mathcal{M}}$, ψ_M, $\nabla\varphi$, and $\mathbf{P}_M$ are now evaluated at $\mathbf{X}_0$. We extend to complex-valued variations as follows. Define the complex-valued vector fields

$$\boldsymbol{\xi} = \boldsymbol{\xi}_1 + i\boldsymbol{\xi}_2, \quad \eta = \eta_1 + i\eta_2, \tag{65}$$

where i is the imaginary number and $\boldsymbol{\xi}_\alpha$ and η_α are real-valued. Let overlines denote the complex conjugate. We derive the identity

$$\nabla_Z\eta\cdot\nabla_Z\overline{\eta} = \nabla_Z(\eta_1 + i\eta_2)\cdot\nabla_Z(\eta_1 - i\eta_2) = \nabla_Z\eta_1\cdot\nabla_Z\eta_1 + \nabla_Z\eta_2\cdot\nabla_Z\eta_2, \tag{66}$$

i.e., the imaginary part vanishes. Similarly, one can show that

$$\nabla_Z\boldsymbol{\xi}\cdot\boldsymbol{\mathcal{M}}\left[\nabla_Z\overline{\boldsymbol{\xi}}\right] = \nabla_Z\boldsymbol{\xi}_1\cdot\boldsymbol{\mathcal{M}}\left[\nabla_Z\boldsymbol{\xi}_1\right] + \nabla_Z\boldsymbol{\xi}_2\cdot\boldsymbol{\mathcal{M}}\left[\nabla_Z\boldsymbol{\xi}_2\right], \tag{67}$$

and

$$\begin{aligned}(l^2/2)(\nabla\varphi\cdot\nabla_Z\overline{\eta})\mathbf{P}_M\cdot\nabla_X\boldsymbol{\xi} + (l^2/2)(\nabla\varphi\cdot\nabla_Z\eta)\mathbf{P}_M\cdot\nabla_X\overline{\boldsymbol{\xi}} \\ = l^2(\nabla\varphi\cdot\nabla_Z\eta_1)\mathbf{P}_M\cdot\nabla_X\boldsymbol{\xi}_1 + l^2(\nabla\varphi\cdot\nabla_Z\eta_2)\mathbf{P}_M\cdot\nabla_X\boldsymbol{\xi}_2.\end{aligned} \tag{68}$$

Equation (67) follows from the major symmetry of $\boldsymbol{\mathcal{M}}$, that is, $\mathbf{A}\cdot\boldsymbol{\mathcal{M}}[\mathbf{B}]=\mathbf{B}\cdot\boldsymbol{\mathcal{M}}[\mathbf{A}]$ for arbitrary tensors $\mathbf{A},\mathbf{B}$. Therefore, if (64) holds for real-valued $\{\eta,\boldsymbol{\xi}\}$, it must also hold for $\{\eta_1,\boldsymbol{\xi}_1\}$ and $\{\eta_2,\boldsymbol{\xi}_2\}$, which by (66), (67), and (68) implies we must have

$$\begin{aligned}&\int_{\mathcal{D}}\left[(l^2/2)\left(\nabla_Z\eta\cdot\nabla_Z\overline{\eta}\right)\psi_M+\nabla_Z\boldsymbol{\xi}\cdot\boldsymbol{\mathcal{M}}[\nabla_Z\overline{\boldsymbol{\xi}}]\right]dV_Z\\+&\int_{\mathcal{D}}\left[(l^2/2)(\nabla\varphi\cdot\nabla_Z\overline{\eta})\mathbf{P}_M\cdot\nabla_X\boldsymbol{\xi}+(l^2/2)(\nabla\varphi\cdot\nabla_Z\eta)\mathbf{P}_M\cdot\nabla_X\overline{\boldsymbol{\xi}}\right]dV_Z\geq 0,\end{aligned}\tag{69}$$

where $\boldsymbol{\xi}$ and η are complex-valued variations generally expressible as (65). Next, suppose

$$\boldsymbol{\xi}=\mathbf{a}\exp\left(ik\mathbf{n}\cdot\mathbf{Z}\right)f(\mathbf{Z}),\quad \eta=b\exp\left(ik\mathbf{n}\cdot\mathbf{Z}\right)f(\mathbf{Z}),\tag{70}$$

where $\mathbf{a}$ and $\mathbf{n}$ are real fixed vectors, b is a real scalar, and $f(\mathbf{Z})$ is a real-valued, compactly supported differentiable function in $\mathcal{D}$. Equations (70) represent localized oscillatory perturbations in $\mathbf{Z}$-space to the underlying equilibrium configuration with $\mathbf{n}$ denoting their direction, $\mathbf{a}$ (resp. b) denoting the polarization of the deformation (resp. microbuckling-field) perturbation, k denoting their wavenumber, and $f(\mathbf{Z})$ denoting their localization envelope. Substituting (70) into (69), dividing by k^2, and passing to the short-wavelength limit $k\to\infty$ yields

$$\left[\mathbf{a}\otimes\mathbf{n}\cdot\boldsymbol{\mathcal{M}}[\mathbf{a}\otimes\mathbf{n}]+(l^2/2)\psi_M b^2|\mathbf{n}|^2+l^2(\nabla\varphi\cdot b\mathbf{n})\left\{\mathbf{P}_M\cdot(\mathbf{a}\otimes\mathbf{n})\right\}\right]\int_{\mathcal{D}}f^2dV_Z\geq 0,\tag{71}$$

and since $f(\mathbf{Z})$ is compactly supported in $\mathcal{D}$, it follows that

$$\mathbf{a}\otimes\mathbf{n}\cdot\boldsymbol{\mathcal{M}}[\mathbf{a}\otimes\mathbf{n}]+(l^2/2)\psi_M b^2|\mathbf{n}|^2+l^2(\nabla\varphi\cdot b\mathbf{n})\left\{\mathbf{P}_M\cdot(\mathbf{a}\otimes\mathbf{n})\right\}\geq 0,\tag{72}$$

where we can now drop evaluation of the terms at the material point $\mathbf{X}_0$ owing to its arbitrariness. Equation (72) is the Legendre-Hadamard condition that any energy minimizing-configuration for (26) must necessarily satisfy in κ for any $\mathbf{a}$, b, and $\mathbf{n}$. If, at any point in the body, the condition (72) is violated, the configuration in question does not minimize the energy (26). It is convenient to rewrite (72) in matrix form as

$$\mathfrak{a}\cdot\mathbb{A}\mathfrak{a}\geq 0,\tag{73}$$

where $\mathfrak{a}=[\mathbf{a}\ b]^T$ is an arbitrary four-vector, $\mathbb{A}$ is the four-tensor

$$\mathbb{A}=\begin{bmatrix}\mathbf{A}(\mathbf{n}) & (l^2/2)(\nabla\varphi\cdot\mathbf{n})\left(\mathbf{P}_M\mathbf{n}\right)\\(l^2/2)(\nabla\varphi\cdot\mathbf{n})\left(\mathbf{P}_M\mathbf{n}\right)^T & (l^2/2)\psi_M|\mathbf{n}^2|\end{bmatrix},\tag{74}$$

and $\mathbf{A}(\mathbf{n})$ is the acoustic tensor defined by the equation

$$\mathbf{a}\cdot\mathbf{A}(\mathbf{n})\mathbf{a}=\mathbf{a}\otimes\mathbf{n}\cdot\boldsymbol{\mathcal{M}}[\mathbf{a}\otimes\mathbf{n}].\tag{75}$$

Equation (73) stipulates that the Legendre-Hadamard condition (72) can be verified, for a given constitutive model and equilibrium configuration, by calculating whether the eigenvalues of $\mathbb{A}$, cf. (74), are nonnegative for any $\mathbf{n}$ when evaluated at this state. This calculation is detailed in the supplementary material included with the article for the specific case of energies (38) and (46).

Remark: It is clear from Equation (72) that the gradient regularization of the microbuckling field, which furnishes the latter terms in (72), plays a key role in the stability of the system. Indeed, if $l\to 0$, then the terms in question vanish.

Remark: If we consider (72) with $b=0$, we arrive at the simplified inequality

$$\mathbf{a}\otimes\mathbf{n}\cdot\boldsymbol{\mathcal{M}}[\mathbf{a}\otimes\mathbf{n}]\geq 0.\tag{76}$$

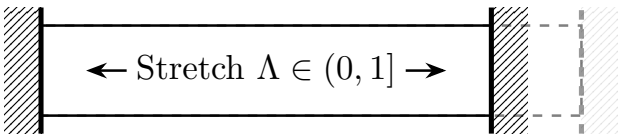

Figure 5: A one-dimensional bar in hard loading conditions.

Equation (76) would recover the standard result in finite elasticity if not for the presence of the microbuckling field φ in the modulus and acoustic tensors. To elaborate, with some work one can derive

$$\boldsymbol{\mathcal{M}} = f_U \boldsymbol{\mathcal{M}}_U + f_M \boldsymbol{\mathcal{M}}_M, \tag{77}$$

where $\boldsymbol{\mathcal{M}}_U = (\psi_U)_{\mathbf{FF}}$ and $\boldsymbol{\mathcal{M}}_M = (\psi_M)_{\mathbf{FF}}$. We interpret the modulus tensor (77) as a linear combination of the moduli relevant to the unbuckled and microbuckled regimes with the functions which quantify their spatial distribution serving as the weighting functions. This result reinforces the notion that the proposed model describes a material whose internal constitution can fluctuate *via* the microbuckling field to achieve energetically-optimal configurations; this is further evidence of its similarity with *pseudo-elasticity* [50].

Remark: Recall from Section 2 that polyconvexity is a sufficient condition for the strict form of (76), that is, (4). It should not be surprising given the above observations that the unified energy (15) is polyconvex if derived from polyconvex constituent energies. The proof follows from the closure of the set of convex functions under non-negative linear combinations. Suppose both ψ_U and ψ_M are polyconvex in which case they are expressible in the general form

$$\Phi = \Phi(\mathbf{F}, \mathbf{F}^*, J), \tag{78}$$

where $\Phi(\cdot,\cdot,\cdot)$ is convex in each argument. By definition, this means that for any $\mathbf{F}_1$ and $\mathbf{F}_2$,

$$\Phi(s\mathbf{F}_1 + (1-s)\mathbf{F}_2, \mathbf{F}^*, J) \leq s\Phi(\mathbf{F}_1, \mathbf{F}^*, J) + (1-s)\Phi(\mathbf{F}_2, \mathbf{F}^*, J), \tag{79}$$

and similarly for the other two arguments. Therefore, the unified energy (15) is expressible as

$$\psi = \Phi_{tot}(\mathbf{F}, \mathbf{F}^*, J) = f_U \Phi_U(\mathbf{F}, \mathbf{F}^*, J) + f_M \Phi_M(\mathbf{F}, \mathbf{F}^*, J), \tag{80}$$

where we also require $f_U \geq 0$ and $f_M \geq 0$, this being already satisfied by (20) and (19), respectively. Using the above results, we find

$$\begin{aligned}
\Phi_{tot}(s\mathbf{F}_1 + (1-s)\mathbf{F}_2, \mathbf{F}^*, J) &= f_U \Phi_U(s\mathbf{F}_1 + (1-s)\mathbf{F}_2, \mathbf{F}^*, J) + f_M \Phi_M(s\mathbf{F}_1 + (1-s)\mathbf{F}_2, \mathbf{F}^*, J) \\
&\leq s f_U \Phi_U(\mathbf{F}_1, \mathbf{F}^*, J) + (1-s) f_U \Phi_U(\mathbf{F}_2, \mathbf{F}^*, J) \\
&+ s f_M \Phi_M(\mathbf{F}_1, \mathbf{F}^*, J) + (1-s) f_M \Phi_M(\mathbf{F}_2, \mathbf{F}^*, J) \\
&= s\Phi_{tot}(\mathbf{F}_1, \mathbf{F}^*, J) + (1-s)\Phi_{tot}(\mathbf{F}_2, \mathbf{F}^*, J),
\end{aligned} \tag{81}$$

i.e., the unified functional Φ_{tot} is also convex in its first argument. Repeating this for the other two arguments concludes the proof.

7 One-dimensional bar

Consider a one-dimensional bar $x \in [0, 1]$ illustrated in Figure 5 in hard loading conditions, *i.e.*, under controlled stretch $\Lambda > 0$, that behaves according to basic quadratic unbuckled and microbuckled energies:

$$\psi_U = \frac{k_U}{2}(\Lambda - 1)^2, \quad \psi_M = \mathcal{G}_M + \frac{k_M}{2}(\Lambda - \Lambda_M)^2. \tag{82}$$

Here, $k_U > k_M > 0$ are stiffness parameters, $\mathcal{G}_M$ is the requisite microbuckling energy, and $\Lambda_M > 0$ is the microbuckled stretch determined *via* the microbuckling criterion (47) as

$$\psi_U(\Lambda_M) = \mathcal{G}_M \implies \Lambda_M = 1 + \sqrt{\frac{2\mathcal{G}_M}{k_U}}. \tag{83}$$

In this setting, stability within each regime is tantamount to strict ordinary convexity whereby the energies satisfy

$$\frac{\partial^2 \psi_U}{\partial \Lambda^2} = k_U > 0, \quad \frac{\partial^2 \psi_M}{\partial \Lambda^2} = k_M > 0. \tag{84}$$

Next, we assume for simplicity that the underlying state is homogeneous and use $f_U = (1-\varphi)^2$ and $f_M = \varphi^2$ to unify the two regimes into a strain energy per unit length:

$$\psi = f_U \psi_U + f_M \left(\mathcal{G}_M + \psi_M\right). \tag{85}$$

Using (20) and (19), we can show that this is convex with respect to Λ and φ independently,

$$\psi'' = 2(\psi_U + \mathcal{G}_M + \psi_M) \geq 0 \quad \text{and} \quad \frac{\partial^2 \psi}{\partial \Lambda^2} = g k_U + f_M k_M \geq 0, \tag{86}$$

where the latter inequality follows from the fact that f_U and f_M are nonnegative functions. However, it remains to determine the condition of stability (3), which is satisfied in this one-dimensional case if the Hessian matrix,

$$\mathbf{H} = \begin{bmatrix} \frac{\partial^2 \psi}{\partial \Lambda^2} & \frac{\partial \psi'}{\partial \Lambda} \\ \text{sym.} & \psi'' \end{bmatrix}. \tag{87}$$

is positive definite. It transpires that this is not the case across all permissible values of the fields (Λ, φ). To see this, we plot in Figure 6 the the stability landscape over the range $\Lambda \times \varphi \in (0,1)\times(0,1)$ for two sets of material parameters. In the left plot, there is a single pocket of stability indicating that an unbuckled material point will be stable for stretches near unity and that a microbuckled material point will be stable for appreciable compressive stretches if not fully microbuckled. In other words, at significant compressive stretches, a fully microbuckled point will actually be unstable while partially microbuckled points will be stable. This indicates that a system governed by the strain energy (85) placed under significant compression could be expected to have a microbuckling field closer to, but not equal to, unity. The right plot depicts the trivial case when the two regimes are indistinguishable and the bar behaves according to the energy

$$\psi(\Lambda, \varphi) = (\Lambda - 1)^2 \eta(\varphi)/2, \tag{88}$$

where $\eta(\varphi) = \varphi^2 + (1-\varphi)^2$. The determinant of the associated Hessian is

$$\det\mathbf{H} = (\Lambda - 1)^2 [\eta\eta'' - 2(\eta')^2]/2. \tag{89}$$

Since $4(\Lambda-1)^2 > 0$, we expect the material stability of the bar to be fully determined by φ through the equation $\eta\eta'' - (\eta')^2$. The roots of this equation are $\varphi = 0.5 \pm 0.29$, with $\eta\eta'' - (\eta')^2 > 0$ within the roots and $\eta\eta'' - (\eta')^2 < 0$ outside of them. Therefore, the bar will be materially stable for $\varphi \in [0.21, 0.79]$ and unstable elsewhere. This conclusion is verified by the numerical results shown in Figure 6. Despite the fact that the two regimes ψ_U and ψ_M are indistinguishable, we have just proven that the bar governed by the energy (85) can still experience instabilities. One explanation for this phenomenon is that, for a fixed compression $\Lambda \in (0,1)$, the total energy of the bar still depends on the microbuckling field through η. This function is positive, convex, and has

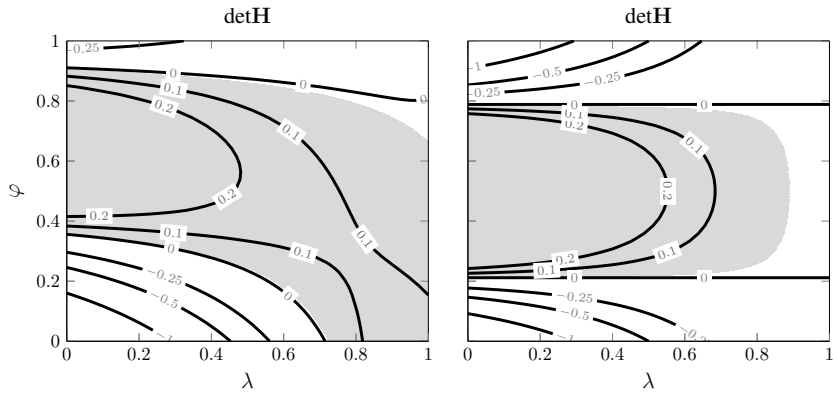

Figure 6: Stability landscape for $\{k_U = 1,\ k_M = 0.4,\ \mathcal{G}_M = 0.01\}$ (left) and $\{k_U = 1,\ k_M = 1,\ \mathcal{G}_M = 0\}$ (right). Gray coloring denotes stable regions according to det$\mathbf{H}$¿0.

a single global minimum at $\varphi = 0.5$. Therefore, the state $\varphi = 0.5$ minimizes the rod's energy. A neighborhood around this minimum, whose size is affected by the choice of f_U and f_M, is adjudged to be stable by the condition det$\mathbf{H} > 0$. This peculiar phenomenon is a consequence of adopting f_U and f_M which do not satisfy the partition of unity, cf. our discussion in Section 4.1.

Remark: The results of this section indicate that a one-dimensional homogeneous bar under hard loading conditions will remain in the unbuckled state until it enters an unstable φ-window, these being illustrated in Figure 6, at which point a localization band would be expected to nucleate. Unlike conventional approaches to one-dimensional material instabilities which rely on intrinsically non-convex energy potentials, *e.g.*, [35], we have demonstrated that instabilities can arise solely from the coupling of strictly convex regimes. The sole *existence* of the microbuckling field renders material instabilities in the system, regardless of the constitutive models used to describe the behavior of the independent regimes.

8 Simulations

We numerically implement the weak form (37) into nonlinear finite elements using the open-source finite element package package FEniCS [70]. Specifically, we identify a suitable finite-dimensional subspace of the trial space $\mathcal{V}_h \times \mathcal{P}_h \subset \mathcal{V} \times \mathcal{P}$ and seek acceptable solutions of the displacement field and microbuckling field $\{\mathbf{u}_h, \varphi_h\} \in \mathcal{V}_h \times \mathcal{P}_h$ to the weak form (37). The field variables are updated using a total additive scheme. The nonlinear system is solved using FEniCS's Newton solver with the direct linear MUMPS solver at each iteration of a given loading increment [71].

We adopt a staggered scheme to solve the coupled system (37) as follows [48, 72]. Consider two solutions $\{\mathbf{u}^{(i)}, \varphi^{(i)}\}$ to the previous loading increment. First, the displacement problem is solved for fixed $\varphi^{(i)}$, yielding $\mathbf{u}^{(i+1)}$. Then, the displacement field in the microbuckling-field problem is updated using this new $\mathbf{u}^{(i+1)}$ and the boundary-value problem is then solved for the new $\varphi^{(i+1)}$. This process is iterated until the following error tolerance is satisfied,

$$\max\left(||\mathbf{u}^{(i+1)} - \mathbf{u}^{(i)}||_{L^2(\kappa)}, ||\varphi^{(i+1)} - \varphi^{(i)}||_{L^2(\kappa)}\right) < \varepsilon_{stag}, \tag{90}$$

indicating that the solution converges within the prescribed tolerance $\varepsilon_{stag} = 10^{-5}$.

l	ρ_{rel}	C_1	C_2	C_7	C_4	C_5	C_6
$L/20$	0.2	1	3/8	0.05	1.4	0.4	3/20

Table 2: Simulation parameters for the uniaxial compression specimen. The results are nondimensionalized by the solid modulus E_s and the specimen length/width L.

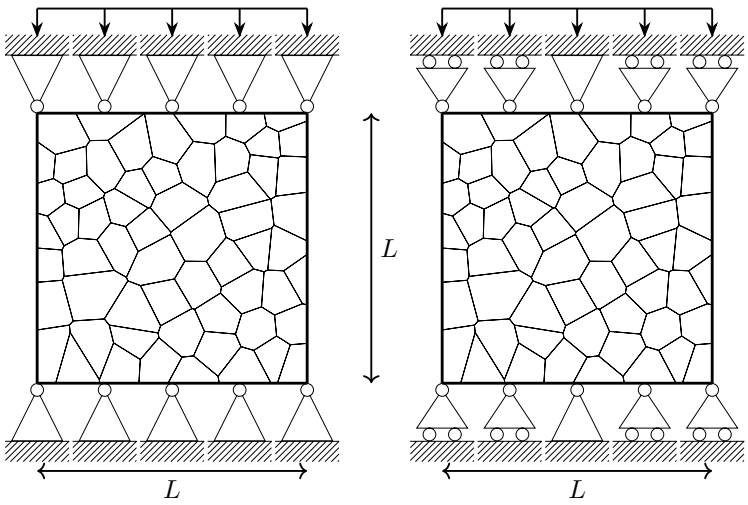

Figure 7: Unconfined uniaxial compression of a canonical cellular solid with fixed (left) and roller (right) supports. The displayed aperiodic microstructure only serves as an illustrative purpose and does not reflect the mesh.

8.1 Uniaxial plane-strain compression

Consider unconfined crushing of a $L \times L$ canonical cellular solid in plane strain conditions. We also suppose the through-thickness is L and we keep L arbitrary because the results will be nondimensionalized accordingly. Referring to Figure 7, we consider two types of boundary conditions: fixed supports on the top and bottom and roller supports on the top and bottom in addition to a fixed central support precluding rigid-body motions. In both cases, we impose a downward vertical displacement on the top boundary over a span of 100 quasistatic increments until a maximum compressive strain of ϵ_D given by (11) is obtained, at which point, by construction *via* (44), the specimen completes densification. We exploit vertical half-symmetry and discretize the right mesh half into a 40×10 crossed mesh of 3-node triangles for a total of 400 elements. A mesh refinement study, described in the supplementary material included with the article, concludes that the results are sufficiently converged for this mesh resolution. The strain energy (56) is used with ψ_U from (38) and ψ_M from (53). We use the canonical empirical fitting constants listed in Table 1 except with $C_7 = 0.05$. The cellular length scale is chosen as $l = L/20$. Note that the system is linearly proportional to E_s pursuant to the remark at the end of Section 5. We scale the reaction force R by the cross-sectional area L^2 to obtain the vertical stress $\sigma = R/L^2$ then scale again by the solid modulus E_s to obtain the nondimensionalized stress $\overline{\sigma} = \sigma/E_s$. The canonical parameters are listed in Table 2.

The nondimensionalized stress-strain curves for both cases are shown in Figure 8 and the deformed configurations, colored by value of the microbuckling field and arranged by the strain amount, are shown in Figure 9. Note the similarity with the canonical response curve in Figure 1. Consider first the fixed support case, which exhibits three distinct regimes: a linearly-elastic

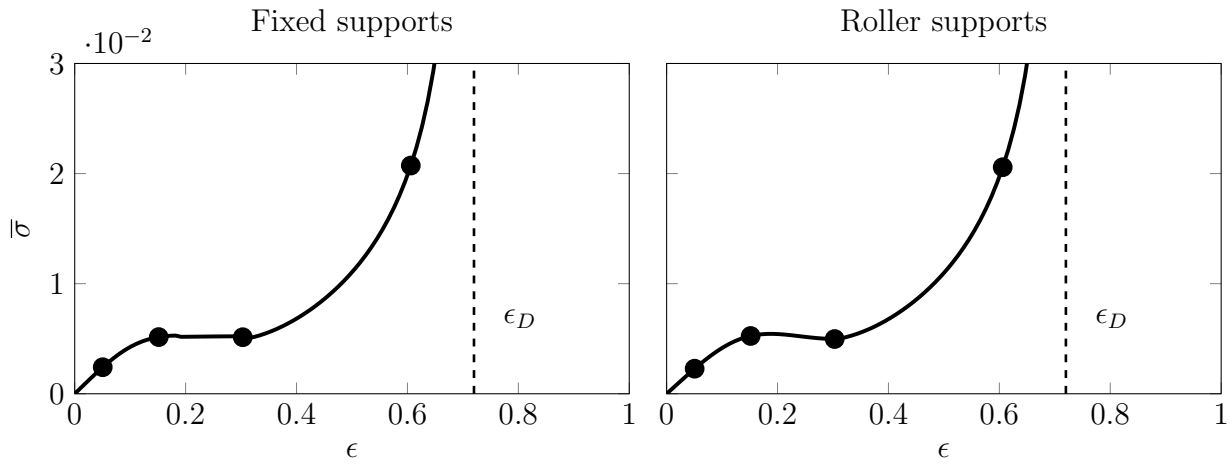

Figure 8: Nondimensionalized stress-strain curves for uniaxial crushing with parameters in Table 2. Curve markers correspond to the values of strain illustrated in Figure 9.

regime, a collapse regime, and a densification regime. This sharp transition occurs because the constrained corner elements experience a stress concentration which makes it energetically favorable for the area to locally microbuckle and cross the energy plateau dividing the two regimes. But since horizontally-adjacent areas would then be subject to a similar stress concentration, they too buckle which culminates in the nucleation of a complete horizontal microbuckling band. This beginning of this band can be seen colored red in Figure 9. This is followed by a prolonged period of dormancy where the stress-strain curve is effectively flat for $\epsilon \in [0.1, 0.3]$. This is consistent with further growth of the microbuckling band whereby the localized bands cascade in the loading direction. Eventually, all of the interior points have locally transitioned to the microbuckled regime. This is consistent with the onset of the densification regime which exhibits a monotonic, nonlinearly-elastic response that diverges as the densification stretch ϵ_D is attained.

For the roller support case, the response curve looks quite similar to the the fixed support case but fails to reproduce the sharp transitions seen in the latter. This is a consequence of not restricting the boundaries horizontally. Since the boundaries are free to expand in the transverse direction, no stress concentrations form which means there is no preferable region for the specimen to microbuckle. As a result, the whole specimen homogeneously transitions between the regimes as illustrated in Figure 9. The roller case differs most from the clamped case during the collapse regime in that microbuckling globally occurs and the curve exhibits folding and clear non-convexity. The response between the two cases then appear to coincide after each specimen is globally microbuckled and densification begins.

Figure 10 illustrates how the specimen's response changes with relative density. In the clamped case, each relative density contour exhibits a distinct linear elastic, collapse, and densification regime. The stress contours increase and diverge at smaller strains with increasing relative density. This is consistent with physical intuition as well as literature studies [3]. The unclamped case similarly diverges with increasing relative density in addition to displaying more and more extreme non-convexity in the response, particularly between the linear elastic and collapse regimes. Further simulations showing how the response changes according to the parameters l, U_{dens}, and C_i are included in the supplementary material. Since the results are normalized by E_s, its effect could be seen simply by scaling $\overline{\sigma}$ by its value.

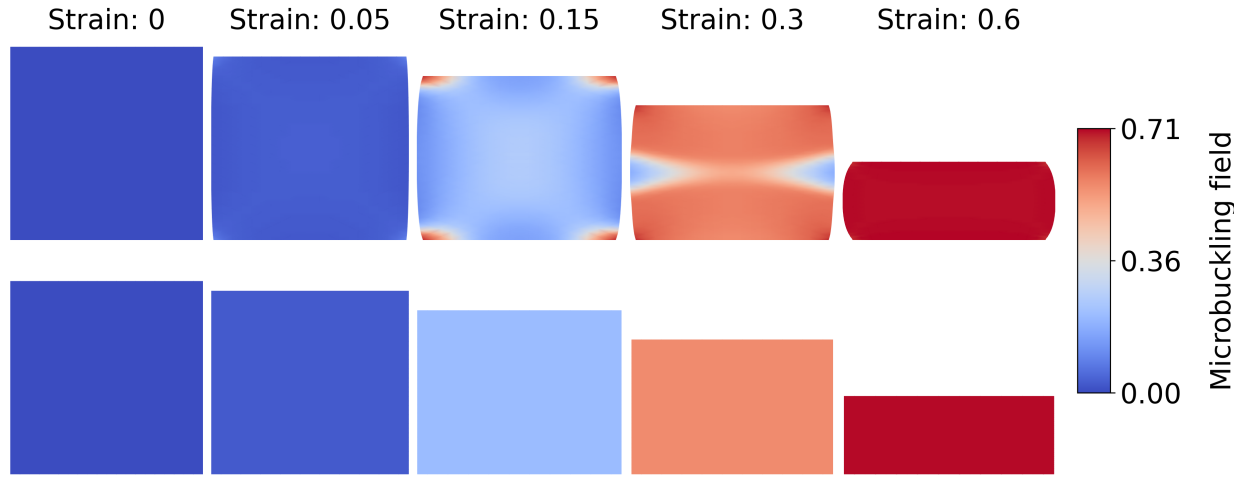

Figure 9: Deformed configurations for fixed (upper) and roller (lower) supports for various compressive strain ϵ.

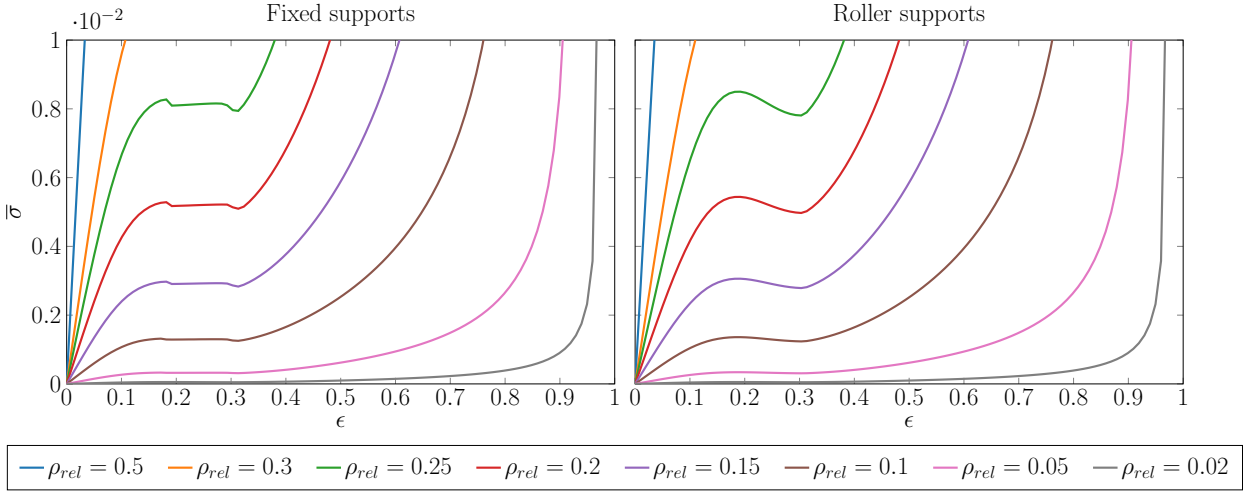

Figure 10: A sweep of relative density with other material parameters in Table 2.

Brand Name	Nickname	L (mm)	E_s (MPa)	ρ_{rel}	l (mm)	C_1	C_2	C_7	C_4	C_5	C_6
EF4005	PU05	25.4	50	0.07	0.2	1.9	0.84	0.07	0.84	0.24	0.20
TF6070-8.5	PU08	25.4	50	0.11	0.2	1.3	0.57	0.06	0.82	0.23	0.23
TF6070-10	PU10	25.4	50	0.13	0.2	1.4	0.59	0.06	0.84	0.24	0.24
TF6070-15	PU15	25.4	50	0.2	0.2	0.85	0.86	0.07	0.80	0.28	0.28

Table 3: Material and empirical parameters for polyurethane foams manufactured by General Plastics.

8.2 Comparison with experimental data

We test the performance of the model by comparing with experimental data for quasistatic unconfined uniaxial compression of four types of elastomeric polyurethane open-celled foams manufactured by General Plastics [73]. Such foams consist of periodically arranged tetrakaidecahedron (Kelvin) cells and are a stereotypical example of a material which exhibits microbuckling [60]. All relevant parameters are listed in Table 3. Each foam was subjected to a compression force deflection (CFD) test in which a 1" cube sample is placed between a rigid substrate and a flat platen which lowers onto the sample and records the force response up to $\epsilon = 0.8$. This is one of many standard test methods for flexible cellular materials standardized by ASTM D3574 and ISO 3386. We simulate the compressive response generated using the known foam material parameters and a good-fit set of empirical fitting parameters C_i from Table 3. We suppose the platens are frictionless for simplicity, and because out-of-plane effects are largely uneventful with elastomeric foams, the plane-strain setup utilized in preceding section is suitable for simulations. Figure 11 shows the experimental data for the four foams in markers and the fitted simulation data in solid lines. The best-fit parameters were generated by hand and are not intended to be true best-fits but rather rough estimates that illustrate a sufficiently good fit for our purposes. Each simulated curve is noticeably faithful to the holistic range of experimental data. We remark that data was not available for $\epsilon > 0.8$, so the tails of the PU05, PU08, and PU10 curves are only estimated.

8.3 Indentation by a flat punch

As a practical problem we show the response of a generic elastomeric foam rectangle being indented by a rigid flat punch in Figure 12. Specifics of the numerical implementation will be presented in an upcoming report. The model requires a relatively coarse mesh and displays clearly rich behavior.

9 Future work

We discuss several avenues for potential further refinement and development of the proposed theory. Owing to the work required to sufficiently analyze the following modifications, we reserve them for future endeavors.

9.1 Energy prescriptions

The kinematic and constitutive developments leading to the general energy prescription (15) included several exploratory modelling choices and assumptions. This includes:

- choosing f_U in (15) in accordance with prevailing phase-field literature;

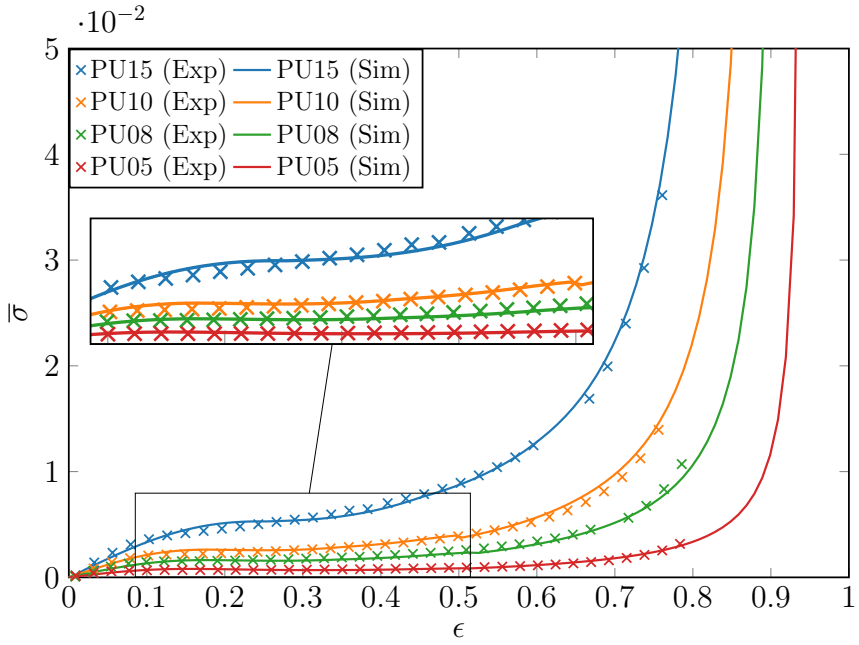

Figure 11: Experimental and simulated reaction curves for polyurethane foams with data in Table 3.

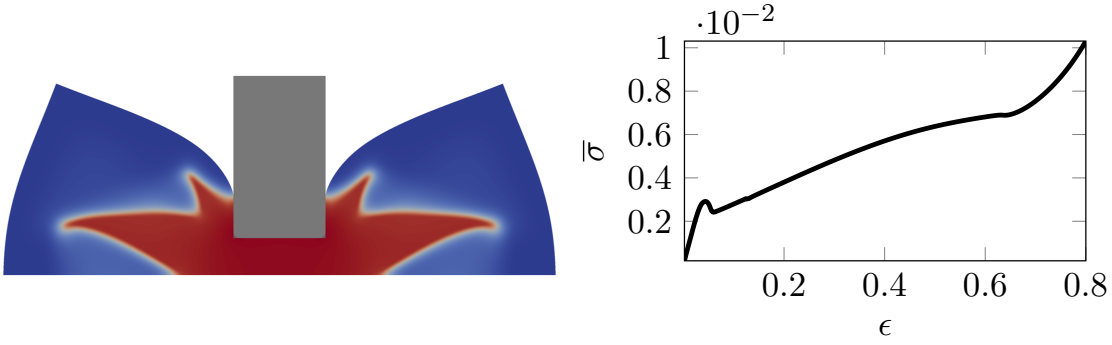

Figure 12: Simulation of square punch indentation colored by value of φ, *cf.* Figure 9.

- casting the transition region as an extension of the microbuckled region and using $\Delta = 1/4$ in (20) in the subsequent extension of f_M to scale it accordingly;
- constructing ψ_M as an an additive combination of a constant microbuckled energy density $\mathcal{G}_M$ and an *ad-hoc* densification energy ψ_M^{dens} in (46);
- postulating $\mathcal{G}_M$ as a novel parameter (41) in the spirit of conventional Gibson-Ashby scaling laws;
- introducing the microbuckling criterion (47) to derive $\mathbf{F}_M$;
- casting $\mathbf{F}_M$ as a zero-energy state of ψ_M in (50) in order to satisfy (49); and
- utilizing an isotropic $\mathbf{F}_M$ (52) in order to make the microbuckling criterion (47) well-posed.

Each of these suppositions undoubtedly had an indelible effect on the results presented in this manuscript and are worthy of further study in their own right. In the future, further work on this formulation could focus on validation or invalidation of these premises in accordance with prevailing physical intuition about these kinds of materials.

9.2 Anisotropic microstructures

Many cellular solids exhibit distinct anisotropy, such as axisymmetry in cork, orthotropy in wood, and hexagonal symmetry in honeycombs. To be a faithful theory, the present model should be modified to account for this directional preference whereby the microbuckling bands nucleate and grow in certain direction as a consequence of the geometry of the underlying microstructure. Since the microbuckling field φ is introduced as an additional kinematic unknown, it should be possible to also introduce into the system an appropriate sense of symmetry with respect to φ. In other words, the cellular symmetry class would induce a material symmetry with respect to φ in the same way that they induce a material symmetry with respect to $\mathbf{F}$. To introduce this concept into the proposed theory, we could leverage tools from conventional material symmetry [44] and anisotropic theories for phase-field fracture [74]. Such efforts could also be useful in modelling microbuckling in transversely-isotropic fiber-reinforced composites, which could be considered a variant of cellular microbuckling and is a significant area of research in its own right [75–77].

9.3 Decoupled microbuckled and interface energies

We expand upon the second item in Section 9.1. As presently written, (15) implies that the width of the transition regime, being regulated by the regularization term in f_M, is associated with the local state of deformation through $\psi_M(\mathbf{F})$. This appeals to no physical intuition – such a transition width more likely represents the geometry of the underlying microstructure and thereby should be agnostic to the material loading. Multiplying φ^2 and $l^2|\nabla\varphi|^2$ by the same energy is reminiscent of the *Ambrosio-Tortorelli* family of Mumford-Shah functionals appearing in the Γ-convergence literature [78]. Alternatively, one could propose strain energies which offer a decoupling of φ^2 and $l^2|\nabla\varphi|^2$, *e.g.*,

$$\psi = f_U\psi_U + f_M\psi_M + f_T\psi_T, \tag{91}$$

where $f_M = \varphi^2$, $f_T = l^2|\nabla\varphi|^2$, and ψ_T corresponds to the energy of the transition or interface region. The prescribed length scale of the transition region l would be effectively subsumed into ψ_T and consequently the transition region may exhibit length scales different than the prescribed l. However, this alternative prescription (91) would permit a user to distinguish between microbuckled and interface energies.

9.4 Dynamic effects

We have said nothing of the dynamical behavior of the proposed system. The transient mechanics of cellular solids constitute an appreciable amount of contemporary engineering research given its relevance to impact mechanics and energy absorption [10,16,79]. Notably, the time scales of loading will inherently dictate whether or not microbuckling occurs. A model which purports to replicate the behavior of such systems should respect this sensitivity. Including viscous effects within this dynamical context can also serve as a convenient means of incorporating rate-dependent microscale dissipation into the system [15].

9.5 Irreversibility

Elastic microbuckling is known to be generally reversible up to hysteresis effects. However, irreversible effects also emerge as a mechanism for microbuckling, *e.g.*, plastic yielding, brittle crushing, and fracture [1]. While the modularity of the unified energy (15) ensures that the particular manifestation of this behavior can be included at the constitutive level using any inelastic models at hand, the irreversibility of the microbuckling field must be ensured in another manner. So-called *history variables* used for enforcing irreversibility in phase-field fracture theory could potentially be useful to this end [80].

10 Conclusions

In this paper we have presented and analyzed a novel model for microbuckling and other material instabilities in general classes of cellular solids such as foams, lattices, and mechanical metamaterials. The model is of a phase-field type and hinges upon the introduction of a novel scalar microbuckling field variable governing whether a material point is locally unbuckled or microbuckled. To this end, two distinct energy regimes are proposed: one corresponding to unbuckled material points and another corresponding to microbuckled and densified material points. Their construction recruits the well-known Gibson-Ashby formulae which calculate the effective macroscale constitutive parameters from the microscale composition and geometry. In this way, the present model is an extension of these algebraic formulae to a variational continuum setting. In contrast to conventional theories for material instabilities, these energies are completely general and need not violate polyconvexity. Indeed, the unification of the two constituent energies into a single energy using the microbuckling field furnishes the potential joint non-convexity which then permits the generation and propagation of localized material behavior. This model was analyzed using both analytical and numerical methods and a rich gamut of possible material behavior was identified for a relatively simple constitutive model. The theory recovers well both localized material instabilities, such as compactly supported microbuckling bands, and global softening mechanisms. Validation of the relatively simple constitutive model with experimental data shows good agreement. In summary, the proposed model aims to fill the exigent lacuna in the literature by proposing a framework that achieves all of the listed goals in Section 1. We have also presented several future means of improving and generalizing the present model including refinement of the energy prescriptions, incorporating cellular anisotropy, alternative unification methods5, dynamic effects, and irreversible microbuckling mechanisms such as plasticity and fracture.

11 Declarations

The author would like to thank Professor Nikolaos Bouklas of Cornell University and Professors Oliver O'Reilly and David Steigmann of UC Berkeley for their helpful comments offered during the writing of this report.

The author is financially supported by a National Science Foundation Graduate Research Fellowship and the Paul R. Gray Distinguished Chair Fund in the College of Engineering at U.C. Berkeley. This support is gratefully acknowledged.

The author declares that they have no conflict of interest.

References

[1] Ashby MF, Medalist RFM. 1983 The Mechanical Properties of Cellular Solids. Metallurgical Transactions A **14**, 1755–1769. (10.1007/BF02645546)

[2] Lakes R. 1993 Materials with Structural Hierarchy. Nature **361**, 511–515. (10.1038/361511a0)

[3] Gibson LJ, Ashby MF. 1997 Cellular Solids: Structure and Properties. Cambridge University Press 2 edition. (10.1017/CBO9781139878326)

[4] Lakes R, Rosakis P, Ruina A. 1993 Microbuckling Instability in Elastomeric Cellular Solids. Journal of Materials Science **28**, 4667–4672. (10.1007/BF00414256)

[5] Gibson L. 1989 Modelling the Mechanical Behavior of Cellular Materials. Materials Science and Engineering: A **110**, 1–36. (10.1016/0921-5093(89)90154-8)

[6] Lakes RS. 2001 Extreme Damping in Composite Materials with a Negative Stiffness Phase. Physical Review Letters **86**, 2897–2900. (10.1103/PhysRevLett.86.2897)

[7] Dykstra DM, Lenting C, Masurier A, Coulais C. 2023 Buckling Metamaterials for Extreme Vibration Damping. Advanced Materials **35**, 2301747. (10.1002/adma.202301747)

[8] Yang H, Ma L. 2019 Multi-Stable Mechanical Metamaterials by Elastic Buckling Instability. Journal of Materials Science **54**, 3509–3526. (10.1007/s10853-018-3065-y)

[9] Jin L, Khajehtourian R, Mueller J, Rafsanjani A, Tournat V, Bertoldi K, Kochmann DM. 2020 Guided Transition Waves in Multistable Mechanical Metamaterials. Proceedings of the National Academy of Sciences **117**, 2319–2325. (10.1073/pnas.1913228117)

[10] Ozdemir Z, Hernandez-Nava E, Tyas A, Warren JA, Fay SD, Goodall R, Todd I, Askes H. 2016 Energy Absorption in Lattice Structures in Dynamics: Experiments. International Journal of Impact Engineering **89**, 49–61. (10.1016/j.ijimpeng.2015.10.007)

[11] Telles R, Mancini JA, Barrera JL, Simoes M, Porcincula DH, Bischoff A, Roach DJ, Leguizamon SC, Lee E, Cook CC, Lewis JA. 2025 Architected Liquid Crystal Elastomer Lattices with Programmable Energy Absorption. Advanced Materials **37**, 2420048. (10.1002/adma.202420048)

[12] Salari-Sharif L, Schaedler TA, Valdevit L. 2014 Energy Dissipation Mechanisms in Hollow Metallic Microlattices. Journal of Materials Research **29**, 1755–1770. (10.1557/jmr.2014.226)

[13] Shan S, Kang SH, Raney JR, Wang P, Fang L, Candido F, Lewis JA, Bertoldi K. 2015 Multistable Architected Materials for Trapping Elastic Strain Energy. Advanced Materials **27**, 4296–4301. (10.1002/adma.201501708)

[14] Findeisen C, Hohe J, Kadic M, Gumbsch P. 2017 Characteristics of Mechanical Metamaterials Based on Buckling Elements. Journal of the Mechanics and Physics of Solids **102**, 151–164. (10.1016/j.jmps.2017.02.011)

[15] Joshi S, Mousavi SM, Hamel CM, Gaitanaros S, Purohit PK, Alberdi R, Bouklas N. 2025 Instabilities and Phase Transformations in Architected Metamaterials: A Gradient-Enhanced Continuum Approach. (10.48550/arXiv.2510.00227)

[16] Barchiesi E, Spagnuolo M, Placidi L. 2019 Mechanical metamaterials: a state of the art. Mathematics and Mechanics of Solids **24**, 212–234. (10.1177/1081286517735695)

[17] Chaudhuri O, Parekh SH, Fletcher DA. 2007 Reversible Stress Softening of Actin Networks. Nature **445**, 295–298. (10.1038/nature05459)

[18] Kim B, Middendorf JM, Diamantides N, Dugopolski C, Kennedy S, Blahut E, Cohen I, Bouklas N, Bonassar LJ. 2022 The Role of Buckling Instabilities in the Global and Local Mechanical Response in Porous Collagen Scaffolds. Experimental Mechanics **62**, 1067–1077. (10.1007/s11340-022-00853-7)

[19] Ciarlet PG. 1988 Mathematical Elasticity. Number v. 20, 27, 29 in Studies in Mathematics and Its Applications. Amsterdam ; New York : New York, N.Y., U.S.A: North-Holland ; Sole distributors for the U.S.A. and Canada, Elsevier Science Pub. Co.

[20] Knowles JK, Sternberg E. 1978 On the Failure of Ellipticity and the Emergence of Discontinuous Deformation Gradients in Plane Finite Elastostatics. Journal of Elasticity **8**, 329–379. (10.1007/BF00049187)

[21] Abeyaratne R, Knowles JK. 2006 Evolution of Phase Transitions: A Continuum Theory. Cambridge University Press 1 edition. (10.1017/CBO9780511547133)

[22] Geymonat G, Müller S, Triantafyllidis N. 1993 Homogenization of Nonlinearly Elastic Materials, Microscopic Bifurcation and Macroscopic Loss of Rank-One Convexity. Archive for Rational Mechanics and Analysis **122**, 231–290. (10.1007/BF00380256)

[23] Geers M, Kouznetsova V, Brekelmans W. 2010 Multi-Scale Computational Homogenization: Trends and Challenges. Journal of Computational and Applied Mathematics **234**, 2175–2182. (10.1016/j.cam.2009.08.077)

[24] Nguyen VD, Noels L. 2014 Computational Homogenization of Cellular Materials. International Journal of Solids and Structures **51**, 2183–2203. (10.1016/j.ijsolstr.2014.02.029)

[25] Van Bree S, Rokoš O, Peerlings R, Doškář M, Geers M. 2020 A Newton Solver for Micromorphic Computational Homogenization Enabling Multiscale Buckling Analysis of Pattern-Transforming Metamaterials. Computer Methods in Applied Mechanics and Engineering **372**, 113333. (10.1016/j.cma.2020.113333)

[26] Glaesener RN, Träff EA, Telgen B, Canonica RM, Kochmann DM. 2020 Continuum Representation of Nonlinear Three-Dimensional Periodic Truss Networks by on-the-Fly Homogenization. International Journal of Solids and Structures **206**, 101–113. (10.1016/j.ijsolstr.2020.08.013)

[27] Bordiga G, Cabras L, Piccolroaz A, Bigoni D. 2021 Dynamics of Prestressed Elastic Lattices: Homogenization, Instabilities, and Strain Localization. Journal of the Mechanics and Physics of Solids **146**, 104198. (10.1016/j.jmps.2020.104198)

[28] Herrnböck L, Steinmann P. 2022 Homogenization of Fully Nonlinear Rod Lattice Structures: On the Size of the RVE and Micro Structural Instabilities. Computational Mechanics **69**, 947–964. (10.1007/s00466-021-02123-0)

[29] Azulay R, Combescure C, Dirrenberger J. 2023 Instability-Induced Pattern Generation in Architectured Materials — A Review of Methods. International Journal of Solids and Structures **274**, 112240. (10.1016/j.ijsolstr.2023.112240)

[30] Azulay R, Combescure C. 2024 Predicting the Post-Bifurcated Patterns of Architectured Materials Using Group-Theoretic Tools. Journal of the Mechanics and Physics of Solids **187**, 105631. (10.1016/j.jmps.2024.105631)

[31] Thbaut M, Audoly B, Lestringant C. 2025 Fixing Non-Positive Energies in Higher-Order Homogenization. Journal of the Mechanics and Physics of Solids **203**, 106168. (10.1016/j.jmps.2025.106168)

[32] Audoly B, Lestringant C, Nassar H. 2025 Classifying Soft Elastic Lattices Using Higher-Order Homogenization. (10.48550/arXiv.2507.00630)

[33] Özdemir I, Brekelmans W, Geers M. 2008 FE^2 Computational Homogenization for the Thermo-Mechanical Analysis of Heterogeneous Solids. Computer Methods in Applied Mechanics and Engineering **198**, 602–613. (10.1016/j.cma.2008.09.008)

[34] Sengupta A, Papadopoulos P, Taylor RL. 2012 A Multiscale Finite Element Method for Modeling Fully Coupled Thermomechanical Problems in Solids. International Journal for Numerical Methods in Engineering **91**, 1386–1405. (10.1002/nme.4320)

[35] Ericksen JL. 1975 Equilibrium of Bars. Journal of Elasticity **5**, 191–201. (10.1007/BF00126984)

[36] Kikuchi N, Triantafyllidis N. 1982 On a Certain Class of Elastic Materials with Nonelliptic Energy Densities. Quarterly of Applied Mathematics **40**, 241–248. (10.1090/qam/678196)

[37] Rosakis P. 1990 Ellipticity and Deformations with Discontinuous Gradients in Finite Elastostatics. Archive for Rational Mechanics and Analysis **109**, 1–37. (10.1007/BF00377977)

[38] Gao DY, Ogden RW. 2008 Multiple Solutions to Non-Convex Variational Problems with Implications for Phase Transitions and Numerical Computation. The Quarterly Journal of Mechanics and Applied Mathematics **61**, 497–522. (10.1093/qjmam/hbn014)

[39] Khajehtourian R, Kochmann DM. 2021 A Continuum Description of Substrate-Free Dissipative Reconfigurable Metamaterials. Journal of the Mechanics and Physics of Solids **147**, 104217. (10.1016/j.jmps.2020.104217)

[40] Rossi N, Méndez C, Huespe A. 2023 Surrogate Model for a Mechanical Metamaterial Undergoing Microstructure Instabilities and Phase Transformations. International Journal of Mechanical Sciences **243**, 107913. (10.1016/j.ijmecsci.2022.107913)

[41] Wagner H. 1929 Ebene Blechwandträger mit sehr dünnen Stegblechen. Zeitschrift für Flugtechnik und Motorluftschiffahrt **20**, 306–315.

[42] Steigmann DJ. 1990 Tension-field theory. Proceedings of the Royal Society of London Series A **429**, 141–173. (10.1098/rspa.1990.0055)

[43] Knops RJ, Wilkes EW. 1973 Theory of Elastic Stability. In Truesdell C, editor, Handbuch der Physik pp. 125–302. Berlin: Springer. (10.1007/978-3-642-69569-8_2)

[44] Steigmann DJ. 2017 Finite Elasticity Theory. Oxford: Oxford University Press.

[45] Noll W. 1958 A Mathematical Theory of the Mechanical Behavior of Continuous Media. Archive for Rational Mechanics and Analysis **2**, 197–226. (10.1007/BF00277929)

[46] Ball JM. 1976 Convexity Conditions and Existence Theorems in Nonlinear Elasticity. Archive for Rational Mechanics and Analysis **63**, 337–403. (10.1007/BF00279992)

[47] Ashby M. 2006 The Properties of Foams and Lattices. Philosophical Transactions of the Royal Society A: Mathematical, Physical and Engineering Sciences **364**, 15–30. (10.1098/rsta.2005.1678)

[48] Abrari Vajari S, Neuner M, Arunachala PK, Linder C. 2023 Investigation of Driving Forces in a Phase Field Approach to Mixed Mode Fracture of Concrete. Computer Methods in Applied Mechanics and Engineering **417**, 116404. (10.1016/j.cma.2023.116404)

[49] Papka SD, Kyriakides S. 1994 In-Plane Compressive Response and Crushing of Honeycomb. Journal of the Mechanics and Physics of Solids **42**, 1499–1532. (10.1016/0022-5096(94)90085-x)

[50] Ogden RW. 2001 Pseudo-Elasticity and Stress Softening. In Fu YB, Ogden RW, editors, Nonlinear Elasticity: Theory and Applications, London Mathematical Society Lecture Note Series, vol. 283, pp. 491–522. Cambridge University Press.

[51] Zienkiewicz O, Taylor R, Fox D. 2014 The Finite Element Method for Solid and Structural Mechanics (Seventh Edition). Oxford: Butterworth-Heinemann.

[52] Tang S, Zhang G, Guo TF, Guo X, Liu WK. 2019 Phase Field Modeling of Fracture in Nonlinearly Elastic Solids via Energy Decomposition. Computer Methods in Applied Mechanics and Engineering **347**, 477–494. (10.1016/j.cma.2018.12.035)

[53] Arriaga M, McAuliffe C, Waisman H. 2015 Onset of Shear Band Localization by a Local Generalized Eigenvalue Analysis. Computer Methods in Applied Mechanics and Engineering **289**, 179–208. (10.1016/j.cma.2015.02.010)

[54] Arriaga M, Waisman H. 2017 Combined Stability Analysis of Phase-Field Dynamic Fracture and Shear Band Localization. International Journal of Plasticity **96**, 81–119. (10.1016/j.ijplas.2017.04.018)

[55] Swamynathan S, Jobst S, Keip MA. 2021 An Energetically Consistent Tension–Compression Split for Phase-Field Models of Fracture at Large Deformations. Mechanics of Materials **157**, 103802. (10.1016/j.mechmat.2021.103802)

[56] dell'Isola F, Steigmann D. 2020 Discrete and Continuum Models for Complex Metamaterials. Cambridge University Press. (10.1017/9781316104262)

[57] Giorgio I, dell'Isola F, Steigmann D. 2018 Axisymmetric Deformations of a 2nd Grade Elastic Cylinder. Mechanics Research Communications **94**, 45–48. (10.1016/j.mechrescom.2018.09.004)

[58] Giorgio I, dell'Isola F, Steigmann DJ. 2024 Second-Grade Elasticity of Three-Dimensional Pantographic Lattices: Theory and Numerical Experiments. Continuum Mechanics and Thermodynamics **36**, 1181–1193. (10.1007/s00161-023-01240-w)

[59] Ciallella A, Steigmann DJ. 2023 Unusual Deformation Patterns in a Second-Gradient Cylindrical Lattice Shell: Numerical Experiments. Mathematics and Mechanics of Solids **28**, 141–153. (10.1177/10812865221101820)

[60] Lakes R. 1995 Experimental Methods for Study of Cosserat Elastic Solids and Other Generalized Elastic Continua. In Mühlhaus H, editor, Continuum Models for Materials with Micro-Structure , pp. 1–22. New York: J. Wiley.

[61] Madeo A, Rémond Y. 2015 Generalized Continuum Mechanics and Engineering Applications. Londres Kidlington: ISTE Press Elsevier.

[62] Steigmann DJ. 2012 Theory of Elastic Solids Reinforced with Fibers Resistant to Extension, Flexure and Twist. International Journal of Non-Linear Mechanics **47**, 734–742.

[63] Eremeyev VA, Lebedev LP, Altenbach H. 2013 Foundations of Micropolar Mechanics. SpringerBriefs in Applied Sciences and Technology. Berlin, Heidelberg: Springer Berlin Heidelberg. (10.1007/978-3-642-28353-6)

[64] Shirani M, Steigmann DJ. 2022 Cosserat Elasticity of Lattice Solids. Journal of Elasticity **151**, 73–88. (10.1007/s10659-021-09859-z)

[65] McAvoy RC, Steigmann DJ. 2024a Cosserat Elasticity of Helically Wound Cylinders. Journal of Elasticity **155**, 205–220. (10.1007/s10659-022-09934-z)

[66] McAvoy R, Steigmann D. 2024b Incremental Deformations and Bifurcation of Elastic Solids Reinforced by Fibers with Intrinsic Extensional, Flexural, and Torsional Elasticity. Journal of Applied Mechanics pp. 1–23. (10.1115/1.4067151)

[67] McAvoy RC. 2025 Consistent Linearization of Micromorphic Continuum Theories. Mathematics and Mechanics of Solids **30**, 1366–1392. (10.1177/10812865241280280)

[68] McAvoy RC. 2025-04 Exotic Buckling Patterns in Fiber-Reinforced Materials: Numerical Simulations of Cosserat Elasticity. International Journal of Solids and Structures **312**, 113272. (10.1016/j.ijsolstr.2025.113272)

[69] Giaquinta M, Hildebrandt S. 2004 Calculus of Variations I vol. 310Grundlehren der mathematischen Wissenschaften. Berlin, Heidelberg: Springer Berlin Heidelberg. (10.1007/978-3-662-03278-7)

[70] Alnæs M, Blechta J, Hake J, Johansson A, Kehlet B, Logg A, Richardson C, Ring J, Rognes ME, Wells GN. 2015 The FEniCS Project Version 1.5. Archive of Numerical Software **Vol 3**, Starting Point and Frequency: Year: 2013 . (10.11588/ANS.2015.100.20553)

[71] Amestoy P, Duff IS, Koster J, L'Excellent JY. 2001 A Fully Asynchronous Multifrontal Solver Using Distributed Dynamic Scheduling. SIAM Journal on Matrix Analysis and Applications **23**, 15–41.

[72] Hirshikesh, Natarajan S, Annabattula RK, Martínez-Pañeda E. 2019 Phase Field Modelling of Crack Propagation in Functionally Graded Materials. Composites Part B: Engineering **169**, 239–248. (10.1016/j.compositesb.2019.04.003)

[73] Long KN, Hamel CM, Waymel R, Bolintineanu DS, Quintana EC, Kramer SL. 2020 Room Temperature Quasi-static Characterization and Constitutive Model Parametrization of Flexible Polyurethane Foams of Different Densities Loaded in Different Orientations. Technical report Sandia National Laboratories (SNL-NM), Albuquerque, NM (United States). (10.2172/1673821)

[74] Teichtmeister S, Kienle D, Aldakheel F, Keip MA. 2017 Phase Field Modeling of Fracture in Anisotropic Brittle Solids. International Journal of Non-Linear Mechanics **97**, 1–21. (10.1016/j.ijnonlinmec.2017.06.018)

[75] Fleck NA, Budiansky B. 1991 Compressive Failure of Fibre Composites Due to Microbuckling. In Dvorak GJ, editor, Inelastic Deformation of Composite Materials , pp. 235–273. New York, NY: Springer New York. (10.1007/978-1-4613-9109-$8_1$2)

[76] Merodio J, Ogden R. 2003 Instabilities and Loss of Ellipticity in Fiber-Reinforced Compressible Non-Linearly Elastic Solids under Plane Deformation. International Journal of Solids and Structures **40**, 4707–4727. (10.1016/S0020-7683(03)00309-3)

[77] López Jiménez F, Pellegrino S. 2012 Folding of Fiber Composites with a Hyperelastic Matrix. International Journal of Solids and Structures **49**, 395–407. (10.1016/j.ijsolstr.2011.09.010)

[78] Ambrosio L, Tortorelli VM. 1990 Approximation of Functional Depending on Jumps by Elliptic Functional via Γ-convergence. Communications on Pure and Applied Mathematics **43**, 999–1036. (10.1002/cpa.3160430805)

[79] Maiti S, Gibson L, Ashby M. 1984 Deformation and energy absorption diagrams for cellular solids. Acta metallurgica **32**, 1963–1975.

[80] Miehe C, Hofacker M, Welschinger F. 2010 A Phase Field Model for Rate-Independent Crack Propagation: Robust Algorithmic Implementation Based on Operator Splits. Computer Methods in Applied Mechanics and Engineering **199**, 2765–2778. (10.1016/j.cma.2010.04.011)